

Fast, Precise Myelin Water Quantification using DESS MRI and Kernel Learning

Gopal Nataraj*, Jon-Fredrik Nielsen[†], Mingjie Gao*, and Jeffrey A. Fessler*

*Dept. of Electrical Engineering and Computer Science, University of Michigan

[†]Dept. of Biomedical Engineering, University of Michigan

Abstract

Purpose: To investigate the feasibility of myelin water content quantification using fast dual-echo steady-state (DESS) scans and machine learning with kernels.

Methods: We optimized combinations of steady-state (SS) scans for precisely estimating the fast-relaxing signal fraction f_F of a two-compartment signal model, subject to a scan time constraint. We estimated f_F from the optimized DESS acquisition using a recently developed method for rapid parameter estimation via regression with kernels (PERK). We compared DESS PERK f_F estimates to conventional myelin water fraction (MWF) estimates from a longer multi-echo spin-echo (MESE) acquisition in simulation, in vivo, and ex vivo studies.

Results: Simulations demonstrate that DESS PERK f_F estimators and MESE MWF estimators achieve comparable error levels. In vivo and ex vivo experiments demonstrate that MESE MWF and DESS PERK f_F estimates are quantitatively comparable measures of WM myelin water content. To our knowledge, these experiments are the first to demonstrate myelin water images from a SS acquisition that are quantitatively similar to conventional MESE MWF images.

Conclusion: Combinations of fast DESS scans can be designed to enable precise f_F estimation. PERK is well-suited for f_F estimation. DESS PERK f_F and MESE MWF estimates are quantitatively similar measures of WM myelin water content.

Keywords: myelin imaging, Bayesian experiment design, DESS, machine learning, kernel regression

Funding Information: National Institutes of Health grant P30 AG053760, University of Michigan MCubed seed grant, University of Michigan predoctoral fellowship

Submitted to Magnetic Resonance in Medicine

1 Introduction

Myelin is a lipid-rich material that forms an insulating sheath encasing neuronal axons predominantly in white matter (WM) regions of the human brain [1]. Demyelination (*i.e.*, myelin loss) is central to the development of several neurodegenerative disorders such as multiple sclerosis (MS) [2]. Non-invasive myelin quantification in WM is thus desirable for monitoring the onset and progression of neurodegenerative disease.

MR relaxation time constants (especially spin-spin time constant T_2) depend on the macromolecular environment surrounding water molecules. In nerve tissue, these environments vary spatially on scales much smaller than the millimeter-scale resolutions used in typical MR imaging experiments. Many researchers have attempted to characterize nerve tissue microstructure by estimating the intravoxel distribution of MR relaxation time constants and associating certain ranges of time constants with particular “compartments” or “pools” of water molecules that exist in similar macromolecular environments. In vitro NMR studies of nerve animal tissue ascribed a fast-relaxing water compartment with $T_2 \sim 10\text{-}40\text{ms}$ initially to general protein and phospholipid structures [3] and later more specifically to water trapped between the phospholipid bilayers of myelin [4, 5]. Shortly thereafter, the first MR images of so-called *myelin water fraction* (MWF), defined as the proportion of MR signal arising from the fast-relaxing water compartment relative to total MR signal, were demonstrated in vivo in the human brain [6]. More recently, MWF has been shown to correlate well with histological measurements of myelin content in animal models of nerve injury [7] and demyelination [8]. In humans, MWF has been measured to be significantly lower in “normally appearing” WM of MS patients versus controls [9], and to correlate strongly with post-mortem histological measurements of myelin content in MS patients [10]. These studies provide growing evidence that MWF as defined in [6] is a specific quantitative marker of intact WM myelin content.

All of the aforementioned studies estimate MWF images from a multi-echo spin echo (MESE) MRI pulse sequence [11] with long repetition time $T_R \geq 2\text{s}$ to ensure sufficient recovery of the longitudinal magnetization in nerve tissue. Whole-brain MWF imaging using such long- T_R MESE acquisitions at a typical imaging resolution would require hours of scan time. To enable more clinically practical scan times, researchers have more recently shown that MESE-based MWF imaging can be accelerated without significantly changing the resulting MWF images [12, 13] by acquiring multiple gradient echoes per refocusing pulse [14]. However, these and other acquisition modifications used in [13] do not address the fundamental long- T_R requirement of MESE acquisitions and thus would still require long scan times for whole-brain MWF imaging at millimeter-scale resolution. Furthermore, estimating a T_2 distribution from MESE data constitutes a poorly conditioned estimation problem that continues to demand high SNR [15, 16], so the need remains for a more SNR-efficient acquisition for myelin water imaging. As an alternative to MESE acquisitions, scan profiles consisting of short- T_R steady-state (SS) sequences were proposed for whole-brain myelin water imaging in about 30m scan time [17]. Despite more recent further refinements [18, 19], myelin water images from SS pulse sequences have thus far been shown to be incomparable with MWF images from MESE pulse sequences [20], likely due at least in part to insufficient precision [21] for reasonable scan times.

Inspired by [22], we reconsidered myelin water imaging from SS pulse sequences from the perspective of statistical experiment design. In [22], we optimized several combinations of spoiled gradient-recalled echo (SPGR) [23] and dual-echo steady-state (DESS) scans [24, 25] for single-

compartment T_1, T_2 estimation and found that different optimized scan combinations produced significantly different in vivo T_2 estimates (but comparable phantom T_2 estimates), indicating in vivo sensitivity to model non-idealities. Further simulation studies suggested that these inconsistencies may be attributable to multi-compartmental relaxation. This paper demonstrates that this apparent SPGR/DESS sensitivity to multi-compartmental relaxation can be exploited for fast, precise myelin water imaging.

This paper introduces a new method¹ for myelin water content quantification based on a fast SS MRI acquisition and PERK [28], a recently developed learning-inspired algorithm for fast, scalable MRI parameter estimation. The acquisition consists of a combination of DESS scans optimized to enable precise estimation of the fast-relaxing signal fraction f_F in two-compartment signal models, subject to a total scan time constraint. The PERK estimator learns a globally optimal regression function that nonlinearly maps DESS measurements to f_F estimates using simulated training points, kernel functions, and convex optimization. Our precision-optimized DESS acquisition is as fast as the SS acquisition proposed in [18] but enables $\sim 40\%$ expected coefficient of variation in unbiased f_F estimates. (Similar calculations for [17, 18] found that f_F coefficients of variation frequently exceeded 100% [21].) In vivo and ex vivo experiments demonstrate that DESS PERK f_F estimates and conventional MESE MWF estimates are quantitatively comparable measures of WM myelin water content. To our knowledge, these experiments are the first to demonstrate myelin water images from a SS acquisition that are quantitatively similar to MESE MWF images.

2 Theory

This section highlights several unconventional aspects of our myelin water imaging framework. §2.1 describes a two-compartment DESS signal model. §2.2 develops a scalable method for scan optimization. §2.3 overviews Parameter Estimation via Regression with Kernels (PERK) [26, 28], a recently developed machine learning algorithm for fast multiple-parameter estimation.

2.1 A Two-Compartment DESS Signal Model

We assume that MR signal arises from two intra-voxel water compartments: a fast-relaxing compartment characterized by comparatively short spin-lattice $T_{1,F}$ and spin-spin $T_{2,F}$ relaxation times and a slow-relaxing compartment characterized by longer relaxation times $T_{1,S}, T_{2,S}$. If these compartments are allowed to exchange, the resulting DESS signal models are difficult to express exactly² (unlike analogous SPGR [30] or balanced steady-state free precession [31] models) due to strongly time-dependent off-resonance effects imparted by unbalanced DESS dephasing gradients. We focus here on the non-exchanging case for simplicity (as is also commonly done in MESE MWF imaging).

¹This paper substantially extends our previous work in myelin water imaging. Conference paper [26] introduced the estimation algorithm used herein but presented simulation results only. Conference proceeding [27] introduced the experimental design algorithm used herein but did not compare results against conventional MESE MWF estimates.

²However, we have derived approximate two-compartment DESS models [29, Ch. 6] in the presence of first-order exchange.

Assuming the DESS echoes are acquired at symmetric echo times $t \leftarrow \mp T_E$ before and after a near-instantaneous RF pulse centered at time $t \leftarrow 0$ (where \leftarrow denotes assignment), we have shown [29, Ch. 6] through an analysis similar to those in [17, 30] that the non-exchanging noiseless DESS signals can, to within constants, be intuitively written as a sum over compartmental signal contributions:

$$s_D(-T_E) \propto -im_0 \tan \frac{\alpha}{2} \quad (1)$$

$$\begin{aligned} & \times \left(f_F (1 - \eta(T_{1,F}, T_{2,F})) e^{+(1/T_{2,F} - R'_{2,F} + i\omega_F)T_E} \right. \\ & \left. + (1 - f_F)(1 - \eta(T_{1,S}, T_{2,S})) e^{+(1/T_{2,S} - R'_{2,S} + i\omega_S)T_E} \right); \end{aligned}$$

$$s_D(+T_E) \propto +im_0 \tan \frac{\alpha}{2} \quad (2)$$

$$\begin{aligned} & \times \left(f_F \left(1 - \frac{\eta(T_{1,F}, T_{2,F})}{\xi(T_{1,F})} \right) e^{-(1/T_{2,F} + R'_{2,F} + i\omega_F)T_E} \right. \\ & \left. + (1 - f_F) \left(1 - \frac{\eta(T_{1,S}, T_{2,S})}{\xi(T_{1,S})} \right) e^{-(1/T_{2,S} + R'_{2,S} + i\omega_S)T_E} \right), \end{aligned}$$

where η, ξ are intermediate functions defined as

$$\begin{aligned} \eta(t', t'') & := \sqrt{\frac{1 - (\exp(-T_R/t''))^2}{1 - (\exp(-T_R/t')/\xi(t'))^2}}; \\ \xi(t') & := \frac{1 - \exp(-T_R/t') \cos \alpha}{\exp(-T_R/t') - \cos \alpha}. \end{aligned} \quad (3)$$

Here, $f_F \in [0, 1]$ denotes fast-relaxing compartmental fraction; m_0 denotes total spin density; $R'_{2,F}, R'_{2,S}$ and ω_F, ω_S respectively denote compartment-specific broadening bandwidths and median off-resonance frequencies; α denotes flip angle; and T_R denotes repetition interval. These expressions assume that off-resonance distributions are independent across compartments, with Cauchy-distributed marginals. Though this is perhaps a strong assumption, it serves to clearly demonstrate that unlike in the single-compartment case [22, Eq. 17], off-resonance effects may not be aggregated into an apparent spin density – in fact, uncompensated off-resonance terms to first order would influence the apparent compartmental fractions of typical interest.

2.2 A Bayesian Approach to Acquisition Design

This subsection develops our approach to designing a fast SS acquisition that enables precise f_F estimation. For clarity in presentation, we describe the method here in a general manner and provide implementation details in §3.1. Our method is related to the Bayesian Cramér-Rao Bound [32], which has been applied previously in quantitative MRI [33, 34] though with a different cost function than the one developed in this section. We propose an intuitive cost function that is amenable to gradient-based optimization and is thus suitable for multi-dimensional parameter estimation problems.

After image reconstruction, many quantitative MRI acquisitions produce at each voxel position a sequence of measurements $\mathbf{y} \in \mathbb{C}^D$, modeled here as

$$\mathbf{y} = \mathbf{s}(\mathbf{x}, \boldsymbol{\nu}, \mathbf{P}) + \boldsymbol{\epsilon}. \quad (4)$$

Here, $\mathbf{s} : \mathbb{R}^{L+K+AD} \mapsto \mathbb{C}^D$ models D noiseless signals; $\mathbf{x} \in \mathbb{R}^L$ denotes L latent (i.e., unknown) parameters; $\boldsymbol{\nu} \in \mathbb{R}^K$ denotes K known parameters; $\mathbf{P} \in \mathbb{R}^{A \times D}$ collects A acquisition parameters for each of D measurements; and $\boldsymbol{\epsilon} \sim \mathcal{CN}(\mathbf{0}_D, \boldsymbol{\Sigma})$ denotes complex Gaussian noise with zero mean $\mathbf{0}_D \in \mathbb{R}^D$ and known covariance $\boldsymbol{\Sigma} \in \mathbb{R}^{D \times D}$. (As a concrete example, for single-compartment T_2 estimation from spin echo measurements, \mathbf{x} could collect m_0, T_2 ; $\boldsymbol{\nu}$ could collect known main and RF transmit field inhomogeneities; and \mathbf{P} could collect D echo times.) We seek to design \mathbf{P} to enable precise estimation of one or more elements of \mathbf{x} .

We approach acquisition design by minimizing a cost function that characterizes estimation imprecision. To develop this cost function, we utilize the Cramér-Rao Bound [35], which states that the covariance of any unbiased estimator of \mathbf{x} is bounded below by the inverse (if it exists) of the Fisher information matrix

$$\mathbf{F}(\mathbf{x}, \boldsymbol{\nu}, \mathbf{P}) := (\nabla_{\mathbf{x}} \mathbf{s}(\mathbf{x}, \boldsymbol{\nu}, \mathbf{P}))^H \boldsymbol{\Sigma}^{-1} \nabla_{\mathbf{x}} \mathbf{s}(\mathbf{x}, \boldsymbol{\nu}, \mathbf{P}), \quad (5)$$

where $\nabla_{\mathbf{x}}$ denotes row gradient with respect to \mathbf{x} and $(\cdot)^H$ denotes conjugate transpose. We focus on minimizing a weighted average of latent parameter variance lower bounds

$$\Psi(\mathbf{x}, \boldsymbol{\nu}, \mathbf{P}) := \text{tr}(\mathbf{W} \mathbf{F}^{-1}(\mathbf{x}, \boldsymbol{\nu}, \mathbf{P}) \mathbf{W}) \quad (6)$$

where $\text{tr}(\cdot)$ denotes the matrix trace operation and $\mathbf{W} \in \mathbb{R}^{L \times L}$ is a diagonal weighting matrix. Directly optimizing (6) over \mathbf{P} would encourage precise estimation only for some specific $\mathbf{x}, \boldsymbol{\nu}$ values. In [22], we addressed this dependence of Ψ on $\mathbf{x}, \boldsymbol{\nu}$ through a min-max optimization problem. The associated ‘‘worst-case’’ design criterion required relatively mild assumptions on the distribution of $\mathbf{x}, \boldsymbol{\nu}$ but was non-differentiable in \mathbf{P} . For the lower-dimensional application studied in [22], we optimized the min-max criterion through exhaustive grid search, so non-differentiability did not matter. However, grid search scales poorly with D and $D \geq L$ for well-conditioned estimation, so the need for an alternative approach increases for higher- L estimation problems. We study here an alternate design criterion that is amenable to gradient-based optimization. Specifically, we seek \mathbf{P} that minimizes the *expected* weighted average of latent parameter variance lower bounds over an acquisition parameter design search space \mathbb{P} :

$$\mathbf{P}^* \in \left\{ \arg \min_{\mathbf{P} \in \mathbb{P}} \bar{\Psi}(\mathbf{P}) \right\}, \text{ where} \quad (7)$$

$$\bar{\Psi}(\mathbf{P}) := \mathbb{E}_{\mathbf{x}, \boldsymbol{\nu}}(\Psi(\mathbf{x}, \boldsymbol{\nu}, \mathbf{P})) \quad (8)$$

and $\mathbb{E}_{\mathbf{x}, \boldsymbol{\nu}}(\cdot)$ denotes joint expectation with respect to a prior joint distribution on $\mathbf{x}, \boldsymbol{\nu}$. Under certain conditions (detailed in the Appendix), expected cost $\bar{\Psi}$ is differentiable in \mathbf{P} and is thus amenable to gradient-based local optimization.

2.3 PERK: A Fast Algorithm for Multiple-Parameter Estimation

This subsection overviews PERK, a fast machine learning algorithm for dictionary-free per-voxel MRI parameter estimation. PERK is a computationally efficient alternative to conventional dictionary-

based grid search estimation: specifically, PERK may scale better than grid search with the number of unknowns (see §S-II and §S-III respectively for supporting results and discussion). We recently developed and demonstrated PERK for single-compartment T_1, T_2 estimation [28] and a full description is provided therein. Here we review the PERK estimator at a conceptual level; the Appendix reviews selected mathematical details and §S-I explains our implementation for myelin water imaging.

In essence, PERK learns a simple nonlinear estimator from simulated labeled training points and evaluates the learned estimator on unlabeled test data. PERK first samples prior parameter and noise distributions and evaluates signal model (4) many times to form a set of parameter-measurement tuples. The goal of PERK is to then learn from these labeled training points a suitable estimator that maps each measurement and known parameter realization to a reasonable latent parameter estimate. This supervised learning problem is subject to a tradeoff between expressivity and training complexity: more complicated estimator architectures have the potential to accurately represent a larger space of functions but are computationally harder to train. Towards good expressivity, researchers have recently proposed to learn deep neural network architectures for quantitative MRI [36, 37]. However, it is well known that deep learning requires enormous numbers of training points to train many hyperparameters without overfitting, and its limited theoretical basis renders its practical use largely an art. PERK instead learns a much simpler estimator architecture that is a weighted combination of nonlinear *kernel* functions. For appropriate kernel choices, the PERK estimator is uniquely and globally optimal over a very diverse function space, so PERK enjoys good expressivity despite its simple form. We previously demonstrated good PERK performance for single-compartment T_1, T_2 estimation from SS [26, 28] and MR fingerprinting data [38]; the results herein suggest that PERK is suitable for higher-dimensional estimation problems as well.

3 Methods

This section describes our myelin water imaging experiments. §3.1 applies Bayesian scan design (*cf.* §2.2) to design a fast combination of SPGR and DESS scans that enables precise f_F estimation. Interestingly, the optimized acquisition consists only of DESS scans (see §5 for discussion of this). §3.2, §3.3, and §3.4 describe comparisons respectively in simulation, in vivo, and ex vivo studies of PERK f_F estimates from the optimized DESS acquisition to nonnegative least-squares (NNLS) and regularized NNLS (RNNLS) conventional MWF f_M estimates from a MESE acquisition. §S-I provides PERK and conventional estimator implementation details. In the interest of reproducible research, code and data will be freely available at <https://github.com/gopal-nataraj/mwf>.

3.1 Acquisition Design

We assumed identical broadening distributions across compartments (*i.e.*, $R'_{2,F} \equiv R'_{2,S}$ and $\omega_F \equiv \omega_S$) to simplify scan design optimization. Specifically, this simplification enabled generation via the MATLAB[®] Symbolic Toolbox of cumbersome but analytical expressions for relevant gradients and mixed gradients of the SPGR [30] and DESS (1)-(2) magnitude signal models. We used magnitude signal models to reduce SPGR/DESS signal dependence on off-resonance effects, noting that Rician distributed noise in corresponding magnitude image data is well-approximated as

Gaussian for sufficiently large SNR [39]. We modeled each flip angle $\alpha \leftarrow \alpha_0 \kappa$ to deviate from a nominal prescribed value α_0 by spatially-varying transmit field sensitivity $\kappa \approx 1$. We fixed T_E across scans and thereby reduced model dependencies to seven free object parameters per voxel: $f_F, T_{1,F}, T_{2,F}, T_{1,S}, T_{2,S}, \kappa$, and $c := m_0 e^{-R'_{2,F} T_E} \equiv m_0 e^{-R'_{2,S} T_E}$; and two acquisition parameters per dataset: $\mathbf{p}_d \leftarrow [\alpha_0, T_R]^T, \forall d \in \{1, \dots, D\}$. We assumed prior knowledge of transmit field sensitivity $\nu \leftarrow \kappa$ (that in experiments we estimated from separate fast acquisitions [40]-[41]) and collected the remaining $L \leftarrow 6$ latent parameters as $\mathbf{x} \leftarrow [f_F, T_{1,F}, T_{2,F}, T_{1,S}, T_{2,S}, c]$.

We took fast-relaxing compartmental fraction f_F to be a quantitative measure of myelin water content and tailored scan design problem (7) to encourage scan combinations that enable precise f_F estimation. Specifically, we set weight matrix $\mathbf{W} \leftarrow \text{diag}((E_{\mathbf{x},\nu}(f_F))^{-1}, \mathbf{0}_5)$ to penalize f_F imprecision only. Here, fast-fraction variance weight $(E_{\mathbf{x},\nu}(f_F))^{-1}$ assigns interpretable meaning to $\sqrt{\bar{\Psi}(\mathbf{P})}$ as a unitless measure of the expected coefficient of variation afforded by \mathbf{P} in asymptotically unbiased estimates of f_F .

We approximated expectations of form $E_{\mathbf{x},\nu}(\cdot)$ by taking empirical averages using samples of \mathbf{x}, ν drawn from a prior distribution. We used a coordinate-wise separable prior distribution, modeling $f_F \sim \text{unif}(0.03, 0.21)$ to conservatively contain state-of-the-art MESE MWF measurements in WM [20] and modeling $T_{1,F}, T_{2,F}, T_{1,S}$, and $T_{2,S}$ to be Gaussian distributed with means 400ms, 20ms, 1000ms, and 80ms selected from literature measurements [6, 18] and standard deviations that are 20% of corresponding means. Since \mathbf{W} placed zero weight on estimating c , it sufficed to fix $c \leftarrow 1$ and to assign noise variance $\Sigma \leftarrow (1.49 \times 10^{-7}) \mathbf{I}_{10}$ based on separate measurements in unit-normalized image data. Lastly, we modeled $\kappa \sim \text{unif}(0.9, 1.1)$ to account for 10% transmit field variation (simulations demonstrate good performance even with 20% transmit field variation).

We constrained our search space \mathbb{P} to reflect hardware, safety, and model-accuracy limitations and to avoid undesirably long acquisitions. To control RF energy deposition, we restricted DESS flip angles to range between 1° and 60° . We further restricted SPGR flip angles to be between 1° and 40° to avoid excessive model mismatch due to partial spoiling effects [23]. To comply with other fixed pulse sequence timing requirements, we required DESS and SPGR repetition times to be no less than 17.5ms and 11.8ms respectively. We constrained each pair of DESS defocusing- and refocusing-echo datasets to be assigned the same flip angle and repetition time. Lastly, we imposed a somewhat ambitious total scan time constraint $\sum_{d=1}^D T_{R,d} \leq 108\text{ms}$ that ensured all feasible points described acquisitions at least as fast as the state-of-the-art SS acquisition proposed in [18]. These constraints together defined a convex search space over which we optimized $\bar{\Psi}$.

We separately optimized (8) for each of the 25 candidate SPGR/DESS scan combinations that are feasible under the above time constraint and also produce at least 6 measurements (necessary for well-conditioned estimation). For a candidate combination containing D datasets, we separately solved (7) with $200D$ initializations selected uniformly randomly within the feasible set. For each combination and each initialization, we solved (7) using the built-in MATLAB[®] function `fmincon` with the `active-set` algorithm, a maximum of 500 iterations, and otherwise default options. We performed scan optimization running MATLAB[®] R2017a with a pool of 12 workers on two Xeon-X5650 2.67GHz hexa-core CPUs.

Table 1 summarizes the optimized scan parameter $\hat{\mathbf{P}}$ that locally minimizes (8) over all combinations and all initializations. We find that $\sqrt{\bar{\Psi}(\hat{\mathbf{P}})} = 0.425$, meaning that at a realistic noise level, the acquisition defined by $\hat{\mathbf{P}}$ is expected to yield 42.5% coefficient of variation in asymptotically unbiased f_F estimates from non-exchanging two-compartment signal models.

	Optimized flip angles (deg)	Optimized repetition times (ms)
SPGR	–	–
DESS	$[33.0, 18.3, 15.1]^T$	$[17.5, 30.2, 60.3]^T$

Table 1: SPGR/DESS flip angles and repetition times that comprise $\widehat{\mathbf{P}}$, a scan parameter matrix designed under total time budget $\sum_{d=1}^D T_{R,d} \leq 108\text{ms}$ for precise f_F estimation in WM. For our noise variance measurements, this acquisition is expected to yield 42.5% coefficient of variation in asymptotically unbiased f_F estimates from two-compartment signal models. Interestingly, the optimized scan combination consists only of DESS scans.

3.2 Simulation Studies

We simulated data to arise from two non-exchanging water compartments with different fast $T_{2,F} \leftarrow 20\text{ms}$ and slow $T_{2,S} \leftarrow 80\text{ms}$ transverse relaxation time constants (selected based on [6, 18]) but the same bulk longitudinal relaxation time constant $T_1 \leftarrow 832\text{ms}$ in WM and $T_1 \leftarrow 1331\text{ms}$ in GM (selected based on [42]). With this two-compartment ground truth, MWF f_M and fast-relaxing fraction f_F are equivalent, so their estimates are statistically comparable. (§S-II.B describes a more realistic three-compartment study where f_M and f_F are no longer equivalent.) We assigned $f_M \equiv f_F \leftarrow 0.15$ in WM and $f_M \equiv f_F \leftarrow 0.03$ in GM and constrained corresponding slow-compartment fractions as $1 - f_F$. We prescribed these parameter values to the 81st slice of the BrainWeb digital phantom [43] to produce 217×181 ground truth parameter maps. We generated κ to model 20% flip angle spatial variation. Using extended phase graphs to model stimulated echo signal contributions due to non-ideal refocusing, we simulated noiseless single-coil 32-echo MESE image data with nominal 90° excitation and nominal 180° refocusing flip angles; $T_E \leftarrow 10\text{ms}$ echo interval spacing; $T_R \leftarrow 600\text{ms}$ repetition time; and two cycles of gradient dephasing before and after each refocusing pulse. We corrupted noiseless MESE images with additive complex Gaussian noise to yield noisy complex datasets with SNR ranging from 17-868 in WM and 15-697 in GM, where SNR is defined

$$\text{SNR}(\tilde{\mathbf{y}}, \tilde{\boldsymbol{\epsilon}}) := \|\tilde{\mathbf{y}}\|_2 / \|\tilde{\boldsymbol{\epsilon}}\|_2 \quad (9)$$

for image data voxels $\tilde{\mathbf{y}}$ and noise voxels $\tilde{\boldsymbol{\epsilon}}$ corresponding to a region of interest (ROI) within one image.

Using non-exchanging two-compartment models (1)-(2), we also simulated noiseless single-coil DESS image data using the precision-optimized nominal flip angles and repetition times presented in Table 1 and fixed symmetric defocusing and refocusing echo times $T_E \leftarrow 5.29\text{ms}$. We corrupted noiseless DESS images with additive complex Gaussian noise to yield noisy complex datasets with SNR ranging from 22-222 in WM and 25-242 in GM, where SNR is computed via (9).

We performed simulations and experiments running MATLAB[®] R2013a on a 3.5GHz desktop computer with 32GB RAM. We estimated f_M from noisy magnitude MESE images and known T_1, κ maps by solving NNLS (S1) and RNNLS (S2) problems as explained in §S-I.B. We estimated f_F from noisy magnitude DESS images and known κ maps as detailed in §S-I.A. NNLS and RNNLS respectively took 40.3s and 49.6s. PERK training and testing respectively took 33.8s and 1.0s.

3.3 In vivo Studies

We acquired all datasets using the TOPPE pulse sequence prototyping environment [44] on a GE DiscoveryTM MR750 3.0T scanner with a 32-channel Nova Medical[®] receive head array. In a single scan session involving a healthy volunteer, we collected the optimized DESS acquisition described in §3.1; a MESE acquisition for validation; an SPGR acquisition for separate bulk T_1 estimation; and a Bloch-Siegert (BS) acquisition for separate κ estimation. Each of these acquisitions is described next in turn.

We acquired DESS data by prescribing the optimized nominal flip angles and repetition times presented in Table 1 and holding all other scan parameters fixed across DESS scans. For excitation, all acquisitions in this work used a 9.0mm slab-selective Shinnar-Le Roux (SLR) pulse [45] of duration 3.0ms and time-bandwidth product 6. We interleaved RF excitations with 2 gradient dephasing phase cycles over a 3mm slice thickness to distinguish the DESS echoes. We acquired DESS data with a $200 \times 200 \times 8$ matrix over a $240 \times 240 \times 24\text{mm}^3$ field of view (FOV). Using a 31.25kHz readout bandwidth, we acquired 3D axial DESS data at minimum $T_E \leftarrow 5.29\text{ms}$ before and after RF excitations. To avoid slice-profile effects, we sampled k-space over a 3D Cartesian grid. Including time to reach steady-state, the optimized DESS acquisition took 3m15s scan time.

We acquired MESE data with a 90° nominal excitation flip angle, achieved by scaling the same SLR pulse shape as above. A sequence of 32 identical nominally 180° refocusing pulses succeeded each excitation, where the time between excitation and first refocusing pulse peaks was fixed to the minimum possible $\frac{T_E}{2} \leftarrow 4.6\text{ms}$ and subsequent refocusing pulse peaks were separated by echo spacing $T_E \leftarrow 9.2\text{ms}$. We designed each refocusing pulse as a 21.0mm slab-selective SLR pulse of duration 2.0ms and time-bandwidth product 2. We elected to use shaped refocusing pulses instead of shorter hard pulses to suppress unwanted signal outside the excitation slab due to imperfect refocusing. To suppress stimulated echo signal contributions, we flanked each refocusing pulse with a symmetric gradient crusher pair, where each crusher imparted 14 phase cycles across the 21.0mm refocusing slab. Immediately following the refocusing pulse train, we imparted 8 gradient dephasing phase cycles over a 3mm slice thickness to suppress residual transverse magnetization. To reduce scan time, we used a repetition time $T_R \leftarrow 600\text{ms}$ that is shorter than those used in recent works (*e.g.*, [13, 20]) and used separate bulk T_1 estimates (from the SPGR scans described next) to account for incomplete recovery. We acquired 3D MESE data over the same imaging volume and with the same resolution, readout bandwidth, and k-space trajectory as was used for the DESS acquisition. We repeated the MESE scan twice to permit averaging in postprocessing for increased SNR. Including three prepended repetitions to approach steady-state, each MESE scan took 16m2s for a total MESE acquisition time of 32m4s.

We acquired SPGR data for separate bulk T_1 estimation, for the sole purpose of aiding MESE MWF estimation. We varied nominal flip angles from 5° to 45° with 5° increments and fixed all other scan parameters across scans. We acquired 3D data at minimal echo time $T_E \leftarrow 5.1\text{ms}$ and repetition time $T_R \leftarrow 13.1\text{ms}$ over the same imaging volume and with the same resolution, readout bandwidth, and k-space trajectory as was used in the DESS acquisition. We implemented RF spoiling by imparting 8 gradient dephasing phase cycles over a 3mm slice thickness immediately following each readout and by RF phase cycling with a 117° linear RF phase increment [23]. Including time to reach steady-state, the SPGR acquisition took 3m32s scan time.

We acquired a pair of BS-shifted SPGR scans [40] for separate flip angle scaling κ estimation. We modified the 3D SPGR sequence just described by inserting a $\pm 4\text{kHz}$ off-resonant Fermi pulse

(of 9.0ms duration and with 0.05G peak amplitude) immediately following on-resonant excitation and immediately prior to readout. This extended the echo time to $T_E \leftarrow 15.0\text{ms}$. We also conservatively extended the repetition time to $T_R \leftarrow 300\text{ms}$ to prevent excess RF heating. We used a small 5° nominal excitation flip angle for reduced contrast in BS images and thereby smoother κ estimates. We acquired BS data with a reduced $200 \times 50 \times 8$ matrix. All other scan parameters were the same as for the SPGR acquisition. Including time to reach steady-state, the BS acquisition took 4m30s scan time.

We reconstructed all raw coil images via 3D Fourier transform and subsequently processed only one image slice centered within the excitation slab. We upsampled BS coil images along the phase-encoding direction to the same image size as other coil images, using zero-padding to suppress ringing. We jointly coil-combined all coil images using an extension of JSENSE [46] for multiple datasets. We estimated flip angle spatial variation κ maps by normalizing and calibrating regularized transmit field estimates [41] from complex coil-combined BS images. We estimated bulk T_1 maps from magnitude coil-combined SPGR images and κ maps using variable projection method [47] and a one-dimensional grid search over 1000 logarithmically-spaced T_1 samples between 10ms and 3000ms. To address bulk motion between acquisitions, we rigidly registered coil-combined MESE and DESS images as well as κ, T_1 maps to one coil-combined MESE first-echo image. After registration, we averaged MESE images voxel-by-voxel across scan repetitions to increase effective SNR. We estimated f_M from magnitude averaged MESE images and κ, T_1 maps by solving NNLS (S1) and RNNLS (S2) problems as explained in §S-I.B. We estimated f_F from magnitude DESS images and κ maps by applying PERK as explained in §S-I.A. NNLS and RNNLS respectively took 47.2s and 115.4s. PERK training and testing respectively took 35.6s and 0.9s.

3.4 Ex vivo Studies

Ex vivo experiments used a sample from the post-mortem brain of an 81-year-old male with a clinical history of amyotrophic lateral sclerosis (ALS). The brain was fixed in 10% neutral-buffered formalin hours after extraction and was sectioned after two weeks of fixation. We prepared an imaging phantom by submerging a $\sim 1\text{cm}$ -thick sample from the prefrontal cortex in a viscous perfluoropolyether solution (Fomblin Y LVAC 25/6, California Vacuum Technology, Fremont, CA) that does not produce significant MR signal and has been used in other studies (*e.g.*, [48, 49]). To maintain complete immersion and to reduce gradient-induced motion, we anchored the sample at three suture sites to our glass container using nylon thread (marked in Fig. 3). We waited several hours after phantom preparation and before scanning to allow the phantom to equilibrate to scan room temperature.

Similar to in vivo experiments, we acquired DESS, MESE, SPGR, and BS data in a single scan session. We averaged over four MESE scan repetitions and extended MESE repetition interval $T_R \leftarrow 1000\text{ms}$ to further increase effective MESE SNR. We reduced BS repetition interval $T_R \leftarrow 70.4\text{ms}$ since RF heating is of reduced concern here. For all four acquisitions, we collected k -space data over a reduced $200 \times 120 \times 8$ grid and reconstructed images onto a smaller $120 \times 120 \times 24 \text{ mm}^3$ FOV. To accommodate elevated apparent MWF and shorter myelin water T_2 after formalin fixation [50], we trained PERK using modified $f_F, T_{2,F}, T_{2,S}$ marginal distributions $p_{f_F} \leftarrow \text{unif}(-0.1, 0.7)$, $p_{T_{2,F}} \leftarrow \text{logunif}(10, 30)\text{ms}$, and $p_{T_{2,S}} \leftarrow \text{logunif}(30, 300)\text{ms}$. All other data acquisition, image reconstruction, and parameter estimation details were unchanged from in vivo experiments. Each

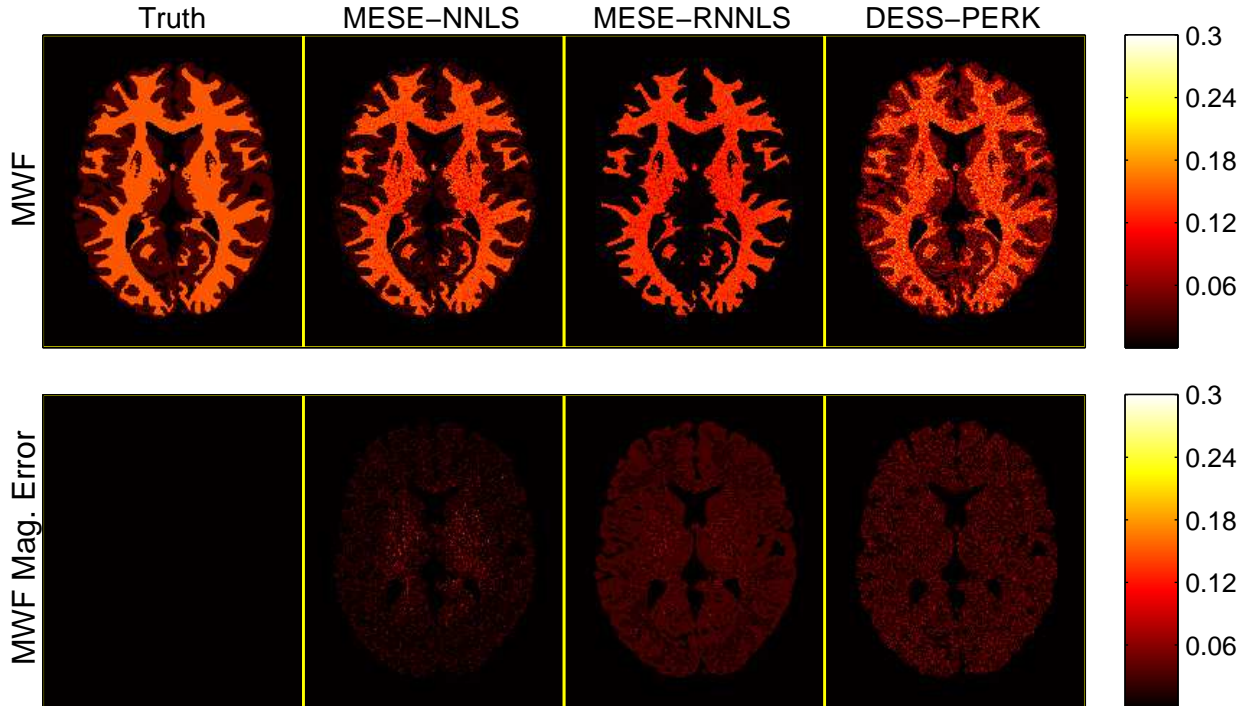


Figure 1: MESE NNLS/RNNLS f_M estimates and DESS PERK f_F estimates alongside corresponding magnitude error images, in a two-compartment simulation. Voxels not assigned WM- or GM-like compartmental fractions are masked out in post-processing for display. Table 2 presents corresponding sample statistics.

MESE repetition took 16m3s for a total MESE acquisition time of 64m12s. DESS, SPGR, BS acquisitions respectively took 1m57s, 2m7s, and 2m32s. NNLS and RNNLS respectively took 28.0s and 34.8s. PERK training and testing respectively took 35.8s and 0.2s.

4 Results

This section demonstrates myelin water imaging using our precision-optimized DESS acquisition (*cf.* §2.2, 3.1) and fast PERK estimation (*cf.* §2.3, S-I.A). §4.1, §4.2, and §4.3 compare DESS PERK f_F estimates to conventional MESE NNLS/RNNLS f_M estimates from the simulation, in vivo, and ex vivo studies respectively described in §3.2, §3.3, and §3.4.

4.1 Simulation Studies

Fig. 1 compares MESE NNLS/RNNLS f_M and DESS PERK f_F estimates alongside magnitude difference images with respect to the ground truth $f_M \equiv f_F$ map. Unlike the DESS f_F estimate, both f_M estimates visibly exhibit systematic error due to flip angle spatial variation despite perfect

	WM	GM
True $f_M \equiv f_F$	0.15	0.03
MESE-NNLS \hat{f}_M	0.1375 ± 0.0187 (0.0225)	0.0203 ± 0.01296 (0.0162)
MESE-RNNLS \hat{f}_M	0.1285 ± 0.0146 (0.0260)	0.00207 ± 0.00524 (0.02841)
DESS-PERK \hat{f}_F	0.1352 ± 0.0267 (0.0305)	0.0436 ± 0.0267 (0.0299)

Table 2: Sample means \pm sample standard deviations (RMSEs) of MESE NNLS/RNNLS f_M estimates and DESS PERK f_F estimates in a two-compartment simulation. Sample statistics are computed over 7810 WM-like and 9162 GM-like voxels. Each sample statistic is rounded off to the highest place value of its (unreported) standard error, computed via formulas in [51]. Fig. 1 presents corresponding images.

knowledge of κ ; this apparent MESE sensitivity to transmit field variation increases in the presence of realistic model mismatch (see §S-II.B).

Table 2 compares sample statistics of MESE NNLS/RNNLS f_M estimates and DESS PERK f_F estimates, computed over 7810 WM-like and 9162 GM-like voxels. Except for the MESE-RNNLS GM f_M estimate, all estimates agree with true values to within one standard deviation. The MESE-NNLS WM and GM f_F estimates achieve the least root mean-squared errors (RMSEs) overall. The RNNLS f_M estimate is more precise but less accurate than the NNLS f_M estimate due to regularization. To better assess whether PERK is suitable for DESS f_F estimation, §S-II.A extends this simulation by adding conventional grid search f_F estimation (that is practical only in simulation).

4.2 In vivo Studies

Fig. 2 compares NNLS and RNNLS f_M estimates from MESE scans as well as PERK f_F estimates from optimized DESS scans. PERK f_F estimates exhibit less WM variation and more clearly delineate cortical WM/GM boundaries than MESE f_M estimates. RNNLS f_M estimates are visibly lower than NNLS f_M estimates due to regularization but exhibit reduced WM variation, somewhat improving visualization of WM tracts. RNNLS f_M and PERK f_F estimates appear visually similar in lateral WM regions, but both NNLS and RNNLS f_M estimates are elevated in medial regions. Elevated MESE f_M estimates in internal capsules (IC) have been attributed to overlapping myelin water and cellular water T_2 peaks in MESE T_2 spectrum estimates [20]. We additionally observe that MESE f_M estimates exhibit similar spatial variation here versus in simulations (*cf.* Figs. S1-S2) suggesting that some spatial variation in MESE f_M estimates may be attributable in part to flip angle variation, despite compensation for transmit field inhomogeneity.

Table 3 summarizes sample statistics of NNLS/RNNLS f_M estimates from MESE scans and PERK f_F estimates from optimized DESS scans, separately computed over four lateral WM ROIs containing 90, 79, 182, and 201 voxels; one pooled medial IC WM ROI containing 347 voxels; and one pooled anterior cortical (AC) GM ROI containing 78 voxels. PERK f_F estimates exhibit the lowest variation within WM ROIs and the most similar sample means across WM ROIs. NNLS and RNNLS f_M sample means are significantly higher in the IC WM ROI than in lateral WM ROIs, possibly due to overlap in NNLS T_2 spectrum peaks and/or to flip angle spatial variation (as described in the previous paragraph). It is challenging to assess quantitative comparability between

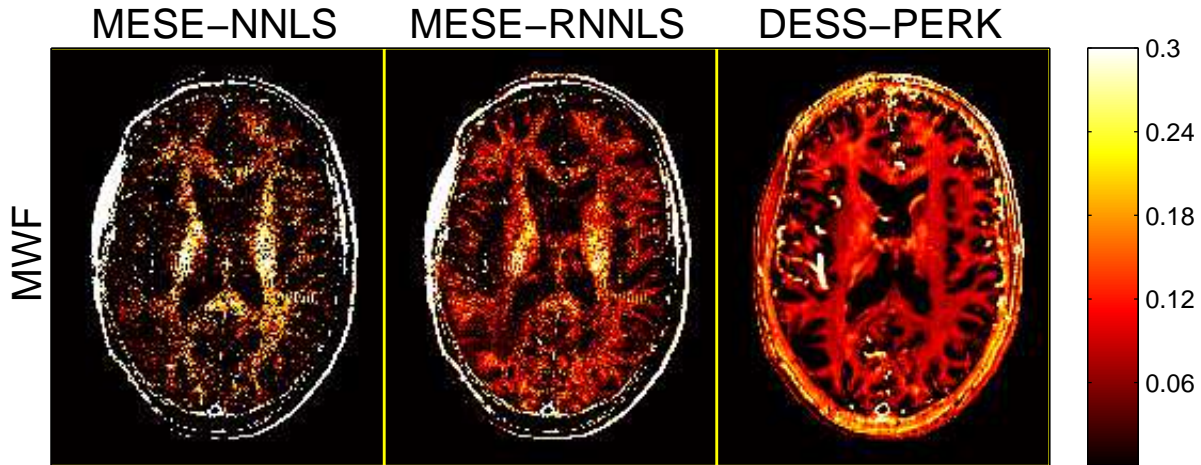


Figure 2: Representative NNLS and RNNLS f_M estimates from a MESE acquisition alongside a PERK f_F estimate from a precision-optimized DESS acquisition, in the brain of a healthy volunteer. Using similar signal reception imaging parameters, MESE f_M estimates took 40m6s total scan time (averaging over two MESE scan repetitions) while DESS f_F estimates took 7m45s total scan time. PERK f_F estimates exhibit less WM variation and more clearly delineate cortical WM/GM boundaries than MESE f_M estimates. Table 3 presents corresponding sample statistics computed over manually selected WM and GM ROIs.

ROI	MESE-NNLS \hat{f}_M	MESE-RNNLS \hat{f}_M	DESS-PERK \hat{f}_F
AR WM	0.081 ± 0.091	0.074 ± 0.054	0.117 ± 0.019
AL WM	0.068 ± 0.086	0.054 ± 0.041	0.100 ± 0.0119
PR WM	0.049 ± 0.075	0.043 ± 0.041	0.093 ± 0.019
PL WM	0.118 ± 0.095	0.075 ± 0.050	0.0870 ± 0.0114
IC WM	0.208 ± 0.133	0.177 ± 0.083	0.111 ± 0.0241
AC GM	0.005 ± 0.020	0.009 ± 0.017	0.019 ± 0.045

Table 3: *Left*: WM/GM ROIs, overlaid on a representative MESE first-echo image. Separate lateral WM ROIs are distinguished by anterior-right (AR), anterior-left (AL), posterior-right (PR), and posterior-left (PL) directions and are respectively comprised of 90, 79, 182, and 201 voxels. Two internal capsule (IC) polygons are pooled into a single medial WM ROI comprised of 347 voxels. Three small anterior cortical (AC) GM polygons are pooled into a single GM ROI comprised of 78 voxels. *Right*: Sample means ± sample standard deviations of NNLS/RNNLS f_M estimates from a MESE acquisition as well as PERK f_F estimates from an optimized DESS acquisition, computed over WM/GM ROIs. Each sample statistic is rounded off to the highest place value of its (unreported) standard error, computed via formulas in [51]. Fig. 2 presents corresponding images.

DESS f_F and MESE f_M ROI sample means due to high within-ROI variation in MESE estimates, though PERK WM f_F sample means agree reasonably with several other methods (*e.g.*, see [15] for a review). Neither the NNLS/RNNLS \hat{f}_M nor PERK \hat{f}_F estimators measured significant myelin

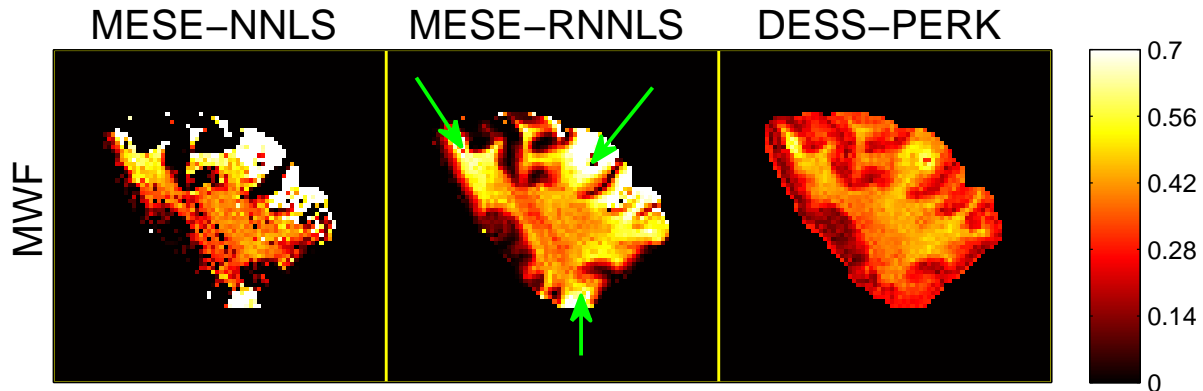


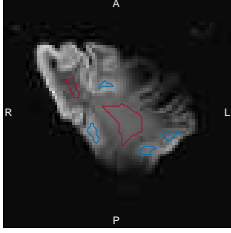
Figure 3: NNLS and RNNLS f_M estimates from a MESE acquisition alongside a PERK f_F estimate in a formalin-fixed sample from the prefrontal cortex of an ALS patient about three weeks after death. Using similar signal reception imaging parameters, MWF f_M estimates took 68m51s total scan time (averaging over four MESE scan repetitions) while DESS f_F estimates took 4m29s total scan time. Green arrows indicate three suture sites used to anchor and stabilize the sample. Warping of the ~ 1 cm-thick sample caused partial-volume effects in the anterior-left and posterior regions (clearly apparent in the anatomical MESE image within Table 4). Away from these regions, MESE f_M and DESS f_F estimates exhibit similar spatial variation and are in reasonable agreement in WM and near WM/GM boundaries. Table 4 presents corresponding sample statistics computed over manually selected WM and GM ROIs.

water content in AC GM.

4.3 Ex vivo Studies

Fig. 3 compares NNLS and RNNLS f_M estimates from MESE scans as well as PERK f_F estimates from optimized DESS scans. All estimates are higher than corresponding in vivo estimates, likely due to formalin fixation [50]. Green arrows mark three suture sites. Warping of the ~ 1 cm-thick sample caused partial-volume effects in anterior-left and posterior regions of this reconstructed slice (see shading in the MESE image within Table 4; adjacent slices contained larger affected regions). Away from suture sites and partial-volume affected regions, MESE f_M and DESS f_F estimates exhibit similar spatial variation and are in reasonable agreement in WM and near WM/GM boundaries. In GM, DESS f_F estimates appear higher than MESE f_M estimates, likely because PERK is here being trained with a sampling distribution support much broader than the prior distribution over which DESS was designed to enable precise f_F estimation. In particular, ex vivo training marginal $p_{f_F} \leftarrow (-0.1, 0.7)$ is much broader than acquisition design prior $f_F \sim \text{unif}(0.03, 0.21)$. Narrowing p_{f_F} to the in vivo range improves agreement across f_F and f_M estimators in ex vivo GM, but degrades PERK performance in ex vivo WM since PERK is then extrapolating well beyond its training distribution.

Table 4 summarizes sample statistics of NNLS/RNNLS f_M estimates from MESE scans and PERK f_F estimates from optimized DESS scans, computed over manually-selected WM and GM ROIs respectively containing 143 and 73 voxels. Within both ROIs, PERK f_F estimates exhibit



ROI	MESE-NNLS \hat{f}_M	MESE-RNNLS \hat{f}_M	DESS-PERK \hat{f}_F
WM	0.366 ± 0.113	0.426 ± 0.061	0.420 ± 0.029
GM	0.08 ± 0.102	0.20 ± 0.14	0.225 ± 0.075

Table 4: *Left*: WM/GM ROIs, overlaid on a representative MESE twelfth-echo image. The WM ROI consists of two manually-selected polygons pooled into a single ROI consisting of 143 voxels. The GM ROI consists of four manually-selected polygons pooled into a single ROI consisting of 73 voxels. *Right*: Sample means \pm sample standard deviations of NNLS/RNNLS f_M estimates from a MESE acquisition as well as PERK f_F estimates from an optimized DESS acquisition, computed over WM/GM ROIs. Each sample statistic is rounded off to the highest place value of its (unreported) standard error, computed via formulas in [51]. Fig. 3 presents corresponding images. Within the WM ROI, MESE f_M and DESS f_F estimates are quantitatively comparable.

the lowest variation. Within the WM ROI, MESE f_M and DESS f_F estimates are quantitatively comparable. Though RNNLS f_M and PERK f_F sample means are similar in GM, it is challenging to quantitatively compare f_M and f_F estimates in GM due to high within-ROI variation in MESE estimates.

5 Discussion

Simulations and experiments demonstrate the feasibility of myelin water content quantification using a precision-optimized DESS MR acquisition and fast machine learning with kernels (PERK). Simulations show that DESS PERK f_F estimators and conventional MESE f_M estimators achieve comparable RMSE in WM- and GM-like voxels. In vivo and ex vivo experiments demonstrate that MESE f_M and DESS f_F estimates are quantitatively comparable measures of WM myelin water content. To our knowledge, these experiments are the first to demonstrate myelin water images from a SS acquisition that are quantitatively similar to conventional MESE MWF images.

Despite freedom to design arbitrary combinations of SPGR and DESS scans, the optimized acquisition used here, as well as several other unreported acquisitions designed under different total time constraints, ended up consisting either entirely or mostly of DESS scans. Since the two-compartment SPGR signal models used in acquisition design depend on $T_{1,F}$, $T_{1,S}$ but not $T_{2,F}$, $T_{2,S}$, DESS-dominated scan designs suggest that multi-compartmental T_2 effects give rise to f_F sensitivity in SS sequences more so than multi-compartmental T_1 effects. Perhaps surprisingly, reported and unreported precision-optimized acquisitions also exhibit substantial T_R diversity across scans, even at the expense of fewer scans than possible under time constraints. In further unreported studies, we investigated this phenomenon by repeating scan optimization while implicitly constraining repetition times to be minimal. We consistently observed substantial (~ 10 -20%) degradation in expected f_F coefficient of variation, suggesting that T_R diversity (in addition to flip angle diversity) is important for designing acquisitions that enable precise f_F estimation.

Our experiments used non-exchanging SPGR and DESS signal models so as to work with closed-form signal models and gradients during acquisition design and to keep consistent with

standard MESE model assumptions. There is growing evidence however that some significant physical exchange across the myelin bilayers likely persists in cerebral WM (*e.g.*, see [16] for a recent review). A thorough investigation of the sensitivity of DESS f_F or MESE f_M estimates to realistic physical exchange rates is a topic for further research.

Even with high SNR, differences in model assumptions, cost functions, and estimation algorithms may limit the quantitative comparability of DESS f_F and MESE f_M imaging as implemented here. For more similar model assumptions, one could attempt to estimate from a suitably optimized DESS acquisition a T_2 (or joint (T_1, T_2)) distribution using two-compartment, three-compartment, or higher-compartment models and correspondingly estimate from MESE data a more coarsely sampled T_2 (or joint (T_1, T_2)) distribution. If κ, T_1 maps are known and non-exchanging additive models are employed, one could estimate T_2 distributions from both MESE and DESS data using NNLS or RNNLS objective functions. With milder model assumptions that cause signal models to be nonlinear in unknowns, one could instead estimate distributions using PERK. This work focused on demonstrating the feasibility of myelin water content quantification using a simple two-compartment model of a fast DESS acquisition; estimating more unknowns from more complicated models will necessitate more scans but could be an interesting area for further research.

6 Conclusion

This paper has introduced a new method for precise myelin water content quantification based on a fast SS acquisition and PERK [28], a fast, scalable machine learning algorithm for MRI parameter estimation. The acquisition consists of three DESS scans whose flip angles and repetition times were optimized under a competitive time constraint to enable precise estimation of the faster-relaxing signal fraction f_F in a two-compartment DESS signal model. Simulations demonstrated that DESS PERK f_F estimators and conventional MESE f_M estimators achieve comparable RMSE in WM- and GM-like voxels. In vivo and ex vivo experiments demonstrated that MESE f_M and DESS PERK f_F estimates are quantitatively comparable measures of WM myelin water content. To our knowledge, these experiments are the first to demonstrate myelin water images from a SS acquisition that are quantitatively similar to conventional MESE MWF images.

Acknowledgments

We thank Roger Albin for initial discussions about neurodegenerative applications, Clay Scott for several discussions about kernel learning, Marina Epelman for a discussion about global optimization for scan design, and Scott Swanson for several discussions about myelin. We also thank the University of Michigan Brain Bank for providing the brain tissue used in ex vivo studies and Tyler Cork for suggesting Fomblin to prepare our ex vivo phantom.

Appendix

Gradient of Bayesian Scan Design Cost

Acquisition design cost $\bar{\Psi}$ is non-convex but typically differentiable in acquisition parameter matrix \mathbf{P} . Here we construct the gradient matrix $\nabla_{\mathbf{P}}\bar{\Psi}(\mathbf{P}) \in \mathbb{R}^{A \times D}$ and provide sufficient conditions for when this gradient matrix exists. Our strategy involves first constructing $\nabla_{\mathbf{P}}\Psi(\mathbf{x}, \boldsymbol{\nu}, \mathbf{P})$ element-wise for fixed $\mathbf{x}, \boldsymbol{\nu}$ and then relating $\nabla_{\mathbf{P}}\bar{\Psi}(\mathbf{P})$ to $\nabla_{\mathbf{P}}\Psi(\mathbf{x}, \boldsymbol{\nu}, \mathbf{P})$. Let $\frac{\partial}{\partial p_{a,d}}$ be the (a, d) th element of matrix operator $\nabla_{\mathbf{P}}$. By standard matrix derivative identities, we have

$$\begin{aligned} \frac{\partial}{\partial p_{a,d}}\Psi(\mathbf{x}, \boldsymbol{\nu}, \mathbf{P}) &\equiv \frac{\partial}{\partial p_{a,d}} \text{tr}(\mathbf{W}\mathbf{F}^{-1}(\mathbf{x}, \boldsymbol{\nu}, \mathbf{P})\mathbf{W}) \\ &= -\text{tr}\left(\mathbf{W}\mathbf{F}^{-1}(\mathbf{x}, \boldsymbol{\nu}, \mathbf{P})\frac{\partial}{\partial p_{a,d}}(\mathbf{F}(\mathbf{x}, \boldsymbol{\nu}, \mathbf{P}))\mathbf{F}^{-1}(\mathbf{x}, \boldsymbol{\nu}, \mathbf{P})\mathbf{W}\right). \end{aligned} \quad (10)$$

If elements of measurement vector \mathbf{y} are assumed to be independent as is typical, Σ takes the form $\Sigma \leftarrow \text{diag}([\sigma_1^2, \dots, \sigma_D^2]^\top)$ and

$$\begin{aligned} \frac{\partial}{\partial p_{a,d}}(\mathbf{F}(\mathbf{x}, \boldsymbol{\nu}, \mathbf{P})) &= \frac{\partial}{\partial p_{a,d}} \sum_{d'=1}^D \frac{1}{\sigma_{d'}^2} (\nabla_{\mathbf{x}} s_{d'}(\mathbf{x}, \boldsymbol{\nu}, \mathbf{p}_{d'}))^H \nabla_{\mathbf{x}} s_{d'}(\mathbf{x}, \boldsymbol{\nu}, \mathbf{p}_{d'}) \\ &= \frac{1}{\sigma_d^2} \frac{\partial}{\partial p_{a,d}} \left((\nabla_{\mathbf{x}} s_d(\mathbf{x}, \boldsymbol{\nu}, \mathbf{p}_d))^H \nabla_{\mathbf{x}} s_d(\mathbf{x}, \boldsymbol{\nu}, \mathbf{p}_d) \right), \end{aligned} \quad (11)$$

where $\text{diag}(\cdot)$ assigns its argument to the diagonal entries of an otherwise zero matrix; and s_d and \mathbf{p}_d respectively denote d th entry of \mathbf{s} and the d th column of \mathbf{P} . Substituting (5) and (11) into (10) gives expressions in terms of signal model derivatives for each element of $\nabla_{\mathbf{P}}\Psi(\mathbf{x}, \boldsymbol{\nu}, \mathbf{P})$. These expressions are well-defined if \mathbf{F} is invertible and if mixed partial derivatives $\nabla_{\mathbf{p}_1}(\nabla_{\mathbf{x}} s_1)^\top, \dots, \nabla_{\mathbf{p}_D}(\nabla_{\mathbf{x}} s_D)^\top$ exist and are continuous in \mathbf{x}, \mathbf{P} , where $(\cdot)^\top$ denotes transpose. Further assuming that $\nabla_{\mathbf{P}}\Psi(\mathbf{x}, \boldsymbol{\nu}, \mathbf{P})$ remains bounded for all $\mathbf{x}, \boldsymbol{\nu}$,

$$\begin{aligned} \nabla_{\mathbf{P}}\bar{\Psi}(\mathbf{P}) &\equiv \nabla_{\mathbf{P}}\mathbb{E}_{\mathbf{x}, \boldsymbol{\nu}}(\Psi(\mathbf{x}, \boldsymbol{\nu}, \mathbf{P})) \\ &= \mathbb{E}_{\mathbf{x}, \boldsymbol{\nu}}(\nabla_{\mathbf{P}}\Psi(\mathbf{x}, \boldsymbol{\nu}, \mathbf{P})), \end{aligned} \quad (12)$$

which provides an expression for the gradient of the expected cost, as desired.

Brief Review of PERK

PERK learns a nonlinear estimator from simulated labeled training points. PERK first samples a prior joint distribution on $\mathbf{x}, \boldsymbol{\nu}$ and evaluates signal model (4) N times (with previously optimized and now fixed acquisition parameter \mathbf{P}^*) to generate sets of parameter and noise realizations $\{\mathbf{x}_1, \boldsymbol{\nu}_1, \boldsymbol{\epsilon}_1\}, \dots, \{\mathbf{x}_N, \boldsymbol{\nu}_N, \boldsymbol{\epsilon}_N\}$ and corresponding measurements $\{\mathbf{y}_1, \dots, \mathbf{y}_N\}$. PERK then seeks to learn from these samples a suitable regression function $\hat{\mathbf{x}}(\cdot) : \mathbb{R}^Q \mapsto \mathbb{R}^L$ that maps each regressor $\mathbf{q}_n := \left[|\mathbf{y}_n|^\top, \boldsymbol{\nu}_n^\top \right]^\top$ to an estimate $\hat{\mathbf{x}}(\mathbf{q}_n)$ that is “close” to corresponding regressand \mathbf{x}_n , where $Q := D + K$ and $n \in \{1, \dots, N\}$. This supervised learning problem is subject to an inherent trade-off between training complexity and estimator accuracy. At one extreme, restricting the estimator

to the affine form $\widehat{\mathbf{x}}(\cdot) \leftarrow \widehat{\mathbf{a}}^\top(\cdot) + \widehat{\mathbf{b}}$ (i.e., affine regression) typically corresponds to well-posed training problem, but an affine estimator is unlikely to be useful when the signal model is nonlinear in \mathbf{x} . At the other extreme, attempting to learn an overly flexible estimator may fail because many candidate regression functions fit any finite N training points with zero training error. PERK balances between these extremes by learning an estimator $\widehat{\mathbf{x}}$ of form $\widehat{\mathbf{x}}(\cdot) \leftarrow \sum_{n=1}^N \widehat{\mathbf{a}} k(\cdot, \mathbf{q}_n) + \widehat{\mathbf{b}}$, where $k : \mathbb{R}^{2Q} \mapsto \mathbb{R}$ is a (typically nonlinear) *reproducing kernel* function [52]. Specifically, the PERK estimator reads

$$\widehat{\mathbf{x}}(\cdot) \leftarrow \mathbf{X} \left(\frac{1}{N} \mathbf{1}_N + \mathbf{M}(\mathbf{M}\mathbf{K}\mathbf{M} + N\rho\mathbf{I}_N)^{-1} \mathbf{k}(\cdot) \right), \quad (13)$$

where $\mathbf{X} := [\mathbf{x}_1, \dots, \mathbf{x}_N]$ collects the regressands; $\mathbf{1}_N \in \mathbb{R}^N$ denotes a vector of ones; $\mathbf{M} := \mathbf{I}_N - \frac{1}{N} \mathbf{1}_N \mathbf{1}_N^\top$ denotes a de-meaning operator; $\mathbf{I}_N \in \mathbb{R}^{N \times N}$ denotes an identity matrix; Gram matrix $\mathbf{K} \in \mathbb{R}^{N \times N}$ consists of entries $k(\mathbf{q}_n, \mathbf{q}_{n'})$ for $n, n' \in \{1, \dots, N\}$; $\rho > 0$ is a regularization parameter; and $\mathbf{k}(\cdot) := [k(\cdot, \mathbf{q}_1), \dots, k(\cdot, \mathbf{q}_N)]^\top - \frac{1}{N} \mathbf{K} \mathbf{1}_N : \mathbb{R}^Q \mapsto \mathbb{R}^N$ is a (typically nonlinear) kernel embedding operator.

PERK estimator (13) is the uniquely and globally optimal regression function within a certain function space whose richness is determined by the choice of kernel, and for good PERK accuracy it is desirable for this function space to be sufficiently diverse. As in [28], we use Gaussian kernel

$$k(\mathbf{q}, \mathbf{q}') \leftarrow \exp \left(-\frac{1}{2} \|\mathbf{q} - \mathbf{q}'\|_{\Lambda^{-2}}^2 \right), \quad (14)$$

where $\Lambda \in \mathbb{R}^{Q \times Q}$ denotes a positive definite bandwidth matrix (that can be selected in a data-driven manner [28]) and $\|\cdot\|_{\Gamma} \equiv \|\Gamma^{1/2}(\cdot)\|$ denotes a weighted ℓ^2 norm for positive semidefinite Γ . For this kernel choice, PERK can approximate \mathcal{L}^2 functions to arbitrary accuracy for N sufficiently large [53].

More challenging applications typically require larger numbers of training samples N , which complicates direct use of PERK estimator (13) due its dependence on dense $N \times N$ Gram matrix \mathbf{K} . Fortunately, Gaussian kernel (14) admits an approximation $k(\mathbf{q}, \mathbf{q}') \approx \mathbf{z}(\mathbf{q})^\top \mathbf{z}(\mathbf{q}') \forall \mathbf{q}, \mathbf{q}'$ [54] that enables constructing $\mathbf{Z} := [\mathbf{z}(\mathbf{q}_1), \dots, \mathbf{z}(\mathbf{q}_N)] \in \mathbb{R}^{Z \times N}$ such that $\mathbf{Z}^\top \mathbf{Z} \approx \mathbf{K}$ for $Z \ll N$, where $\mathbf{z} : \mathbb{R}^Q \mapsto \mathbb{R}^Z$ denotes an approximate nonlinear *feature map* that admits very fast implementation [28]. Substituting low-rank approximation $\mathbf{Z}^\top \mathbf{Z}$ in place of \mathbf{K} in (13) and applying the matrix inversion lemma [55] yields approximate PERK estimator

$$\widehat{\mathbf{x}}(\cdot) \leftarrow \mathbf{m}_x + \mathbf{C}_{xz}(\mathbf{C}_{zz} + \rho\mathbf{I}_Z)^{-1}(\mathbf{z}(\cdot) - \mathbf{m}_z), \quad (15)$$

where $\mathbf{m}_x := \frac{1}{N} \mathbf{X} \mathbf{1}_N$ and $\mathbf{m}_z := \frac{1}{N} \mathbf{Z} \mathbf{1}_N$ are sample means; and $\mathbf{C}_{xz} := \frac{1}{N} \mathbf{X} \mathbf{M} \mathbf{Z}^\top$ and $\mathbf{C}_{zz} := \frac{1}{N} \mathbf{Z} \mathbf{M} \mathbf{Z}^\top$ are sample covariances. Estimator (15) elucidates that Gaussian PERK is approximately equivalent to first nonlinearly transforming regressors $\mathbf{q}_1, \dots, \mathbf{q}_N$ into features $\mathbf{z}(\mathbf{q}_1), \dots, \mathbf{z}(\mathbf{q}_N)$ and then performing regularized affine regression with these (typically higher-dimensional) features; this approximation approaches equality asymptotically in Z .

References

- [1] P. Morell. *Myelin*. Springer, 1984.
- [2] M. M. Goldenberg. Multiple sclerosis review. *Pharmacy and Therapeutics*, 37(3):175–84, March 2012.
- [3] V. Vasilescu, E. Katona, V. Simplaceanu, and D. Demco. Water compartments in the myelinated nerve. III. Pulsed NMR results. *Experientia*, 34(11):1443–4, November 1978.
- [4] R. S. Menon and P. S. Allen. Application of continuous relaxation time distributions to the fitting of data from model systems and excised tissue. *Mag. Res. Med.*, 20(2):214–27, August 1991.
- [5] W. A. Stewart, A. L. Mackay, K. P. Whittall, G. R. W. Moore, and D. W. Paty. Spin-spin relaxation in experimental allergic encephalomyelitis. Analysis of CPMG data using a non-linear least-squares method and linear inverse theory. *Mag. Res. Med.*, 29(6):767–75, June 1993.
- [6] A. Mackay, K. Whittall, J. Adler, D. Li, D. Paty, and D. Graeb. In vivo visualization of myelin water in brain by magnetic resonance. *Mag. Res. Med.*, 31(6):673–7, June 1994.
- [7] P. J. Gareau, B. K. Rutt, S. J. Karlik, and J. R. Mitchell. Magnetization transfer and multi-component T2 relaxation measurements with histopathologic correlation in an experimental model of MS. *J. Mag. Res. Im.*, 11(6):586–95, June 2000.
- [8] S. Webb, C. A. Munro, R. Midha, and G. J. Stanisz. Is multicomponent T2 a good measure of myelin content in peripheral nerve? *Mag. Res. Med.*, 49(4):628–45, April 2003.
- [9] C. Laule, I. M. Vavasour, G. R. W. Moore, J. Oger, D. K. B. Li, D. W. Paty, and A. L. MacKay. Water content and myelin water fraction in multiple sclerosis. *J. Neurol.*, 251(3):284–93, March 2004.
- [10] C. Laule, E. Leung, D. K. B. Li, A. L. Traboulsee, D. W. Paty, A. L. MacKay, and G. R. W. Moore. Myelin water imaging in multiple sclerosis: quantitative correlations with histopathology. *Multiple Sclerosis J.*, 12(6):747–53, November 2006.
- [11] H. Y. Carr and E. M. Purcell. Effects of diffusion on free precession in nuclear magnetic resonance experiments. *Phys. Rev.*, 94(3):630–8, May 1954.
- [12] M. D. Does and J. C. Gore. Rapid acquisition transverse relaxometric imaging. *J. Mag. Res.*, 147(1):116–20, November 2000.
- [13] T. Prasloski, A. Rauscher, A. L. MacKay, M. Hodgson, I. M. Vavasour, C. Laule, and B. Mädler. Rapid whole cerebrum myelin water imaging using a 3D GRASE sequence. *NeuroImage*, 63(1):533–9, October 2012.
- [14] D. A. Feinberg and K. Oshio. GRASE (gradient- and spin-echo) MR imaging: a new fast clinical imaging technique. *Radiology*, 181(2):597–602, November 1991.

- [15] E. Alonso-Ortiz, I. R. Levesque, and G. B. Pike. MRI-based myelin water imaging: A technical review. *Mag. Res. Med.*, 73(1):70–81, January 2015.
- [16] M. D. Does. Inferring brain tissue composition and microstructure via MR relaxometry. *J. Neuroimag.*, 2018.
- [17] S. C. L. Deoni, B. K. Rutt, T. Arun, C. Pierpaoli, and D. K. Jones. Gleaning multicomponent T1 and T2 information from steady-state imaging data. *Mag. Res. Med.*, 60(6):1372–87, December 2008.
- [18] S. C. L. Deoni. Correction of main and transmit magnetic field (B0 and B1) inhomogeneity effects in multicomponent-driven equilibrium single-pulse observation of T1 and T2. *Mag. Res. Med.*, 65(4):1021–35, April 2011.
- [19] S. C. L. Deoni, L. Matthews, and S. H. Kolind. One component? Two components? Three? The effect of including a nonexchanging "free" water component in multicomponent driven equilibrium single pulse observation of T1 and T2. *Mag. Res. Med.*, 70(1):147–54, July 2013.
- [20] J. Zhang, S. H. Kolind, C. Laule, and A. L. MacKay. Comparison of myelin water fraction from multiecho T2 decay curve and steady-state methods. *Mag. Res. Med.*, 73(1):223–32, January 2015.
- [21] C. L. Lankford and M. D. Does. On the inherent precision of mcDESPOT. *Mag. Res. Med.*, 69(1):127–36, January 2013.
- [22] G. Nataraj, J-F. Nielsen, and J. A. Fessler. Optimizing MR scan design for model-based T1, T2 estimation from steady-state sequences. *IEEE Trans. Med. Imag.*, 36(2):467–77, February 2017.
- [23] Y. Zur, M. L. Wood, and L. J. Neuringer. Spoiling of transverse magnetization in steady-state sequences. *Mag. Res. Med.*, 21(2):251–63, October 1991.
- [24] T. W. Redpath and R. A. Jones. FADE-A new fast imaging sequence. *Mag. Res. Med.*, 6(2):224–34, February 1988.
- [25] H. Bruder, H. Fischer, R. Graumann, and M. Deimling. A new steady-state imaging sequence for simultaneous acquisition of two MR images with clearly different contrasts. *Mag. Res. Med.*, 7(1):35–42, May 1988.
- [26] G. Nataraj, J-F. Nielsen, and J. A. Fessler. Dictionary-free MRI parameter estimation via kernel ridge regression. In *Proc. IEEE Intl. Symp. Biomed. Imag.*, pages 5–9, 2017.
- [27] G. Nataraj, J-F. Nielsen, and J. A. Fessler. Myelin water fraction estimation from optimized steady-state sequences using kernel ridge regression. In *Proc. Intl. Soc. Mag. Res. Med.*, page 5076, 2017.
- [28] G. Nataraj, J-F. Nielsen, C. D. Scott, and J. A. Fessler. Dictionary-free MRI PERK: Parameter estimation via regression with kernels. *IEEE Trans. Med. Imag.*, 37(9):2103–14, September 2018.

- [29] G. Nataraj. *Advances in quantitative MRI: acquisition, estimation, and application*. PhD thesis, Univ. of Michigan, Ann Arbor, MI, 48109-2122, Ann Arbor, MI, 2018.
- [30] R. G. Spencer and K. W. Fishbein. Measurement of spin-lattice relaxation times and concentrations in systems with chemical exchange using the one-pulse sequence: breakdown of the Ernst model for partial saturation in nuclear magnetic resonance spectroscopy. *J. Mag. Res.*, 142(1):120–35, January 2000.
- [31] S. C. L. Deoni, B. K. Rutt, and D. K. Jones. Investigating exchange and multicomponent relaxation in fully-balanced steady-state free precession imaging. *J. Mag. Res. Im.*, 27(6):1421–9, June 2008.
- [32] R. D. Gill and B. Y. Levit. Applications of the van Trees inequality: A Bayesian Cramér-rao bound. *Bernoulli*, 1(1/2):59–79, 1995.
- [33] M. Akcakaya, S. Weingartner, Sebastien Roujol, and R. Nezafat. On the selection of sampling points for myocardial T1 mapping. *Mag. Res. Med.*, 73(5):1741–53, May 2015.
- [34] C. M. Lewis, S. A. Hurley, M. E. Meyerand, and C. G. Koay. Data-driven optimized flip angle selection for T1 estimation from spoiled gradient echo acquisitions. *Mag. Res. Med.*, 76(3):792–802, September 2016.
- [35] H. Cramer. *Mathematical methods of statistics*. Princeton Univ. Press, Princeton, 1946.
- [36] P. Virtue, S. X. Yu, and M. Lustig. Better than real: Complex-valued neural nets for MRI fingerprinting. In *Proc. IEEE Intl. Conf. on Image Processing*, pages 3953–7, 2017.
- [37] O. Cohen, B. Zhu, and M. S. Rosen. MR fingerprinting Deep RecOnstruction NEtwork (DRONE). *Mag. Res. Med.*, 80(3):885–94, September 2018.
- [38] G. Nataraj, M. Gao, J. Asslander, C. Scott, and J. A. Fessler. Shallow learning with kernels for dictionary-free magnetic resonance fingerprinting. In *ISMRM Workshop on MR Fingerprinting*, 2017.
- [39] H. Gudbjartsson and S. Patz. The Rician distribution of noisy MRI data. *Mag. Res. Med.*, 34(6):910–4, December 1995.
- [40] L. I. Sacolick, F. Wiesinger, I. Hancu, and M. W. Vogel. B1 mapping by Bloch-Siegert shift. *Mag. Res. Med.*, 63(5):1315–22, May 2010.
- [41] H. Sun, W. A. Grissom, and J. A. Fessler. Regularized estimation of Bloch-Siegert B1+ Maps in MRI. In *Proc. IEEE Intl. Conf. on Image Processing*, pages 3646–50, 2014.
- [42] J. P. Wansapura, S. K. Holland, R. S. Dunn, and W. S. Ball. NMR relaxation times in the human brain at 3.0 Tesla. *J. Mag. Res.*, 9(4):531–8, April 1999.
- [43] D. L. Collins, A. P. Zijdenbos, V. Kollokian, J. G. Sled, N. J. Kabani, C. J. Holmes, and A. C. Evans. Design and construction of a realistic digital brain phantom. *IEEE Trans. Med. Imag.*, 17(3):463–8, June 1998.

- [44] J-F. Nielsen and D. C. Noll. TOPPE: A framework for rapid prototyping of MR pulse sequences. *Mag. Res. Med.*, 79(6):3128–34, June 2018.
- [45] J. Pauly, P. Le Roux, D. Nishimura, and A. Macovski. Parameter relations for the Shinnar-Le Roux selective excitation pulse design algorithm. *IEEE Trans. Med. Imag.*, 10(1):53–65, March 1991.
- [46] L. Ying and J. Sheng. Joint image reconstruction and sensitivity estimation in SENSE (JSENSE). *Mag. Res. Med.*, 57(6):1196–1202, June 2007.
- [47] G. Golub and V. Pereyra. Separable nonlinear least squares: the variable projection method and its applications. *Inverse Prob.*, 19(2):R1–26, April 2003.
- [48] V. V. Itskovich, D. D. Samber, V. Mani, J. G. S. Aguinaldo, J. T. Fallon, C. Y. Tang, V. Fuster, and Z. A. Fayad. Quantification of human atherosclerotic plaques using spatially enhanced cluster analysis of multicontrast-weighted magnetic resonance images. *Mag. Res. Med.*, 52(3):515–23, September 2004.
- [49] R. Symons, T. E. Cork, M. N. Lakshmanan, R. Evers, C. Davies-Venn, K. A. Rice, M. L. Thomas, C-Y. Liu, S. Kappler, S. Ulzheimer, V. Sandfort, D. A. Bluemke, and A. Pourmorteza. Dual-contrast agent photon-counting computed tomography of the heart: initial experience. *Int. J. Cardiovasc. Imaging*, 33(8):1253–61, August 2017.
- [50] A. S. Shatil, M. N. Uddin, K. M. Matsuda, and C. R. Figley. Quantitative ex vivo MRI changes due to progressive formalin fixation in whole human brain specimens: longitudinal characterization of diffusion, relaxometry, and myelin water fraction measurements at 3T. *Frontiers in Medicine*, 5(31):1–15, February 2018.
- [51] S. Ahn and J. A. Fessler. Standard errors of mean, variance, and standard deviation estimators. Technical Report 413, Comm. and Sign. Proc. Lab., Dept. of EECS, Univ. of Michigan, Ann Arbor, MI, 48109-2122, July 2003.
- [52] N. Aronszajn. Theory of reproducing kernels. *Trans. Amer. Math. Soc.*, 68(3):337–404, May 1950.
- [53] I. Steinwart and A. Christmann. *Support vector machines*. Springer, 2008.
- [54] A. Rahimi and B. Recht. Random features for large-scale kernel machines. In *NIPS*, 2007.
- [55] M. A. Woodbury. Inverting modified matrices, 1950. Tech. Report 42, Stat. Res. Group, Princeton Univ.
- [56] G. Nataraj, J-F. Nielsen, M. Gao, and J. A. Fessler. Fast, precise myelin water quantification using DESS MRI and kernel learning, 2018. In preparation.
- [57] M. M. Siddiqui. Statistical inference for Rayleigh distributions. *RADIO SCIENCE Journal of Research NBS/USNC-URSI*, 68D(9):1005–10, September 1964.
- [58] D. Arthur and S. Vassilvitskii. K-means++: The advantages of careful seeding. In *Proc. 18th Annual ACM-SIAM Symp. Disc. Alg. (SODA)*, pages 1027–35, 2007.

- [59] C. L. Lawson and R. J. Hanson. *Solving least squares problems*. Prentice-Hall, 1974.
- [60] R. M. Kroeker and R. M. Henkelman. Analysis of biological NMR relaxation data with continuous distributions of relaxation data. *J. Mag. Res.*, 69(2):218–35, September 1986.
- [61] K. P. Whittall and A. L. MacKay. Quantitative interpretation of NMR relaxation data. *J. Mag. Res.*, 84(1):134–52, August 1989.
- [62] T. Prasloski, B. Mädler, Q-S. Xiang, A. MacKay, and C. Jones. Applications of stimulated echo correction to multicomponent T2 analysis. *Mag. Res. Med.*, 67(6):1803–14, June 2012.
- [63] J. Hennig. Multiecho imaging sequences with low refocusing flip angles. *J. Mag. Res.*, 88(3):397–407, July 1988.

Supporting Information for Fast, Precise Myelin Water Quantification using DESS MRI and Kernel Learning

Gopal Nataraj^{*}, Jon-Fredrik Nielsen[†], Mingjie Gao^{*}, and Jeffrey A. Fessler^{*}

^{*}Dept. of Electrical Engineering and Computer Science, University of Michigan

[†]Dept. of Biomedical Engineering, University of Michigan

This supplement elaborates upon methodology details and presents additional results that were excluded from the main body of the manuscript [56] due to word limits. §S-I details our implementations of PERK and three other estimators used in myelin water imaging experiments. §S-II describes additional simulation studies that investigate reasons for differences between the conventional and proposed myelin water imaging methods. §S-III discusses additional advantages demonstrated by these extended simulations.

S-I Parameter Estimation Implementation Details

S-I.A DESS f_F Estimation

We used data arising from the fast SS scan combination described in Table 1. Since this scan combination consisted of three DESS scans and each DESS scan generates two signals per excitation, this acquisition yielded $D \leftarrow 6$ datasets. We assumed non-exchanging two-compartment DESS signal models (1)-(2) and took the same assumptions as in Subsection 3.1 to reduce model dependencies to $L \leftarrow 6$ latent parameters $\mathbf{x} \leftarrow [f_F, T_{1,F}, T_{2,F}, T_{1,S}, T_{2,S}, c]^T$ and $K \leftarrow 1$ known parameter $\nu \leftarrow \kappa$ per voxel. We focused on precisely estimating f_F in WM from this fast DESS acquisition. We considered the other five latent parameters to be nuisance parameters and thus did not evaluate the performance of their (possibly imprecise) estimators.

In all experiments discussed in the main body, we estimated f_F using approximate PERK estimator (15). We assumed a separable prior distribution $\mathbf{p}_{\mathbf{x},\nu} \leftarrow \mathbf{p}_{f_F} \mathbf{p}_{T_{1,F}} \mathbf{p}_{T_{2,F}} \mathbf{p}_{T_{1,S}} \mathbf{p}_{T_{2,S}} \mathbf{p}_c \mathbf{p}_\kappa$. We set fast-relaxing fraction marginal distribution $\mathbf{p}_{f_F} \leftarrow \text{unif}(-0.1, 0.4)$ and deliberately sample negative values³ with nonzero probability to reduce f_F estimation bias, especially in low- f_F regions. We chose relaxation parameter marginal distributions $\mathbf{p}_{T_{1,F}} \leftarrow \text{logunif}(50, 700)\text{ms}$, $\mathbf{p}_{T_{2,F}} \leftarrow \text{logunif}(5, 50)\text{ms}$, $\mathbf{p}_{T_{1,S}} \leftarrow \text{logunif}(700, 2000)\text{ms}$, $\mathbf{p}_{T_{2,S}} \leftarrow \text{logunif}(50, 300)\text{ms}$ similar to those used for scan design but with finite support. To match the scaling of training and testing data, we set $\mathbf{p}_c \leftarrow \text{unif}(2.2 \times 10^{-16}, u)$, with u set as $10 \times$ the maximum value of magnitude test data. We estimated flip angle scaling marginal \mathbf{p}_κ from known κ map voxels via kernel density estimation (implemented using the built-in MATLAB[®] function `fitdist` with default options)

³Our two-compartment signal models are linear in f_F and are therefore well-defined for zero or even negative f_F values.

and then clipped the support of p_{κ} to assign nonzero probability only within $[0.5, 2]$. We assumed noise covariance Σ of form $\sigma^2 \mathbf{I}_6$ and estimated the (spatially invariant) noise variance σ^2 from Rayleigh-distributed regions of magnitude test data, using estimators described in [57]. We sampled $N \leftarrow 10^6$ latent and known parameter realizations from these distributions and evaluated two-compartment DESS signal models (1)-(2) to generate corresponding complex noiseless measurements. After adding complex Gaussian noise realizations, we concatenated the (Rician) magnitude of these noisy measurements with known parameter realizations to construct pure-real regressors.

We used Gaussian kernel (14) with bandwidth matrix Λ selected as $\Lambda \leftarrow \lambda \text{diag} \left(\left[\mathbf{m}_{|y|}^T, \mathbf{m}_{\nu}^T \right]^T \right)$, where $\mathbf{m}_{|y|} \in \mathbb{R}^D$ and $\mathbf{m}_{\nu} \in \mathbb{R}^K$ denote sample means across voxels of magnitude test image data and known parameters, respectively. We separately selected and then held fixed bandwidth scaling parameter $\lambda \leftarrow 2^{0.3}$ and regularization parameter $\rho \leftarrow 2^{-19}$ via the holdout procedure described in [28]. We implemented a $(Z \leftarrow 10^3)$ -dimensional approximate feature map \mathbf{z} . For training, we used \mathbf{z} to nonlinearly lift regressors into features and then stored $\mathbf{m}_{\mathbf{x}}$, $\mathbf{C}_{\mathbf{xz}}(\mathbf{C}_{\mathbf{zz}} + \rho \mathbf{I}_Z)^{-1}$, and $\mathbf{m}_{\mathbf{z}}$. For testing, we evaluated (15) on test image data and the known transmit field map on a voxel-by-voxel basis.

In the extended simulation study discussed in §S-II, we compared PERK f_F estimates to maximum likelihood (ML) f_F estimates achieved via the variable projection method (VPM) [47] and grid search. Following [22, 28], we clustered known flip angle scaling map voxels into 20 clusters via k -means++ [58] and used each of the cluster means to compute 20 dictionaries. Each of these dictionaries consisted of nearly 8×10^6 signal vectors computed using finely spaced samples on an unrealistically narrow feasible region consisting of a hypercube with boundaries set as $[-0.1, 0.4]$ in f_F and $\pm 20\%$ away from the truth in other latent parameter dimensions. Iterating over clusters, we generated each cluster’s dictionary and applied VPM and grid search over magnitude image data voxels assigned to that cluster.

S-I.B MESE f_M Estimation

We compared f_F estimates from our optimized DESS acquisition to two conventional MWF f_M estimates from a MESE acquisition. The first conventional MWF estimate [6] is related to the solution of a nonnegative least-squares (NNLS) problem [59]

$$\hat{\mathbf{x}}(\mathbf{y}) \in \left\{ \arg \min_{\mathbf{x} \in \mathcal{X}} \|\mathbf{y} - \mathbf{A}\mathbf{x}\|_2^2 \right\}, \quad (\text{S1})$$

where $\mathbf{y} \in \mathbb{R}^D$ here denotes MESE echo amplitudes at D echo times; $\mathbf{A} \in \mathbb{R}^{D \times L}$ models the D MESE signals as weighted sums of L discrete T_2 component signals; $\mathcal{X} \subset \mathbb{R}^L$ is the nonnegative orthant; and $\mathbf{x} \in \mathcal{X}$ here denotes L component weights. Whereas solutions to (S1) tend to be sparse for $L > D$ as is typical, researchers have suggested that spectral distributions are more likely smooth in biological tissue [60]. For smoother in vivo spectrum estimates and for improved problem conditioning, we also compared to a second MWF estimate [61] that is related to the solution of a regularized NNLS problem (RNNLS)

$$\hat{\mathbf{x}}(\mathbf{y}) \in \left\{ \arg \min_{\mathbf{x} \in \mathcal{X}} \|\mathbf{y} - \mathbf{A}\mathbf{x}\|_2^2 + \beta \|\mathbf{x}\|_2^2 \right\}, \quad (\text{S2})$$

where $\beta > 0$ is a regularization parameter. Similar to [6] or [61], each of the two conventional MWF estimators are then respectively defined as $\hat{f}_M := (\mathbf{i}^\top \hat{\mathbf{x}}(\cdot)) / \|\hat{\mathbf{x}}(\cdot)\|_1$, where $\hat{\mathbf{x}}(\cdot)$ is given by (S1) or (S2) and $\mathbf{i} \in \{0, 1\}^L$ is in both cases nonzero only in entries corresponding to $T_2 \in [15, 40]$ ms. As recommended in recent MESE MWF imaging literature [62], we computed MESE signal amplitudes using the extended phase graph (EPG) formalism [63] to account for stimulated echo signal contributions that persist in MESE due to non-ideal refocusing pulses. Note that the conventional EPG-based MESE model ignores exchange. We accounted for non-ideal refocusing by assuming κ is known. We also accounted for incomplete recovery by assuming bulk T_1 is known. To circumvent separate EPG simulations for every voxel, we clustered known κ, T_1 map voxels into 100 clusters via k -means++ [58] and ran 100 EPG simulations using each of the cluster means. Iterating over clusters, we generated each cluster’s system matrix and solved (S1) and (S2) for MESE image voxels assigned to that cluster. We constructed NNLS and RNNLS MWF estimates by estimating $L \leftarrow 100$ spectral component images from $D \leftarrow 32$ MESE measurement images (reducing L did not appreciably influence results). We manually fixed RNNLS regularization parameter $\beta \leftarrow 2^{-13}$ as a small value that provided reasonable in vivo results. We solved (S1) and (S2) using the MATLAB[®] function `lsqnonneg` with default options.

S-II Extensions to Simulation Studies

This section describes additional simulation studies that aid in understanding reasons for differences in MESE f_M and DESS f_F estimates. To help assess whether differences can be explained by the unconventional PERK f_F estimator, §S-II.A extends the two-compartment simulation described in the main body by adding conventional ML f_F estimation. To help assess whether differences can be explained by the idealized two-compartment DESS signal model, §S-II.B investigates estimator performance when voxel data is simulated to more realistically arise from three water compartments.

S-II.A Extension to Two-Compartment Simulation

We extended the two-compartment simulation study described in §3.2 to now include ML f_F estimates (these results were omitted in the main body for consistency across experiments). We estimated f_F from the same noisy magnitude DESS images and the same known κ maps as in the main body, now using the dictionary-based grid search ML estimator described in §S-I.A in addition to the PERK estimator as before. ML estimation took 17726s (nearly 5h). As mentioned in the main body, PERK training and testing respectively took 33.8s and 1.0s.

Fig. S1 extends Fig. 1 by adding the resulting DESS ML f_F estimate alongside a corresponding magnitude difference image with respect to the ground truth $f_M \equiv f_F$ map. The PERK f_F estimate visibly exhibits less error in WM-like voxels than the ML f_F estimate, perhaps in part because PERK tuning parameters (λ, ρ) were optimized via holdout for estimating WM-like f_F values. Both the ML and PERK f_F estimates exhibit less spatial variation in error maps than MESE f_M estimates, suggesting that reduced transmit field sensitivity is not a property of the PERK estimator, but rather due to consideration of transmit field variation during acquisition design.

Table S1 extends Table 2 by adding ML f_F sample statistics. The PERK f_F estimate is more precise but less accurate than the ML f_F estimate because it is a Bayesian estimator [28]. PERK

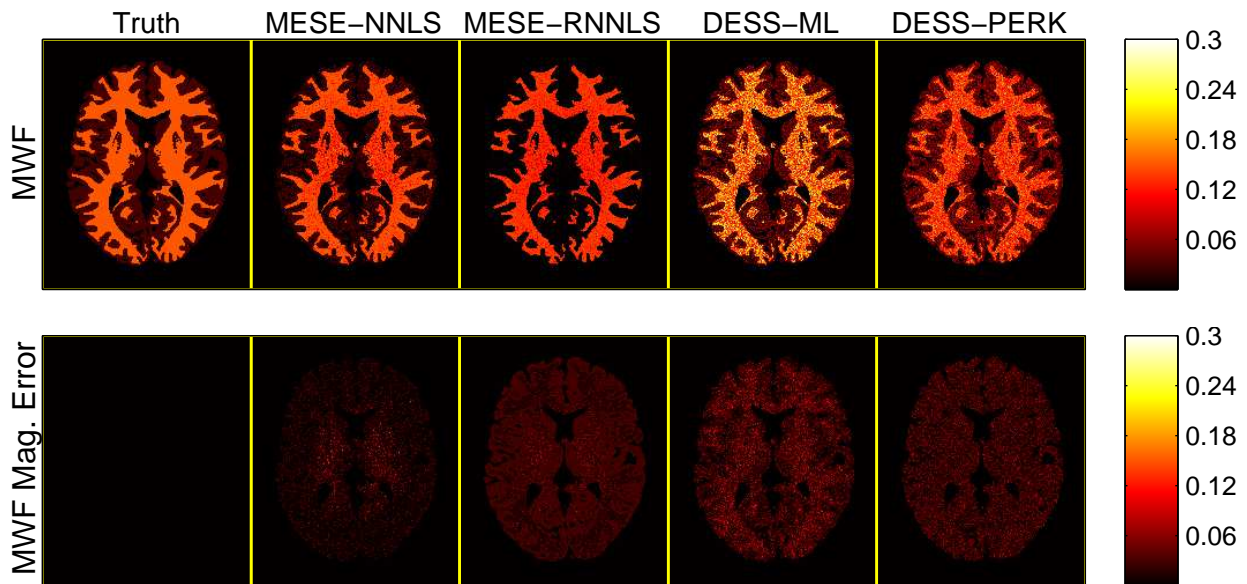


Figure S1: NNLS/RNNLS MESE f_M and ML/PERK DESS f_F estimates alongside corresponding magnitude error images, in a two-compartment simulation where none of the associated estimators incur bias due to model mismatch. Voxels not assigned WM- or GM-like compartmental fractions are masked out in post-processing for display. Table S1 presents corresponding sample statistics.

	WM	GM
True $f_M \equiv f_F$	0.15	0.03
MESE-NNLS \hat{f}_M	0.1375 ± 0.0187 (0.0225)	0.0203 ± 0.01296 (0.0162)
MESE-RNNLS \hat{f}_M	0.1285 ± 0.0146 (0.0260)	0.00207 ± 0.00524 (0.02841)
DESS-ML \hat{f}_F	0.1590 ± 0.0433 (0.0442)	0.0334 ± 0.0272 (0.0274)
DESS-PERK \hat{f}_F	0.1352 ± 0.0267 (0.0305)	0.0436 ± 0.0267 (0.0299)

Table S1: Sample means \pm sample standard deviations (RMSEs) of NNLS/RNNLS MESE f_M estimates and ML/PERK DESS f_F estimates in a two-compartment simulation where none of the associated estimators incur bias due to model mismatch. Sample statistics are computed over 7810 WM-like and 9162 GM-like voxels. Each sample statistic is rounded off to the highest place value of its (unreported) standard error, computed via formulas in [51]. Fig. S1 presents corresponding images.

f_F estimates exhibit better WM RMSE and slightly worse GM RMSE than ML f_F estimates. This extended simulation suggests that PERK is at least as suitable as grid search for reasonable f_F estimation in WM.

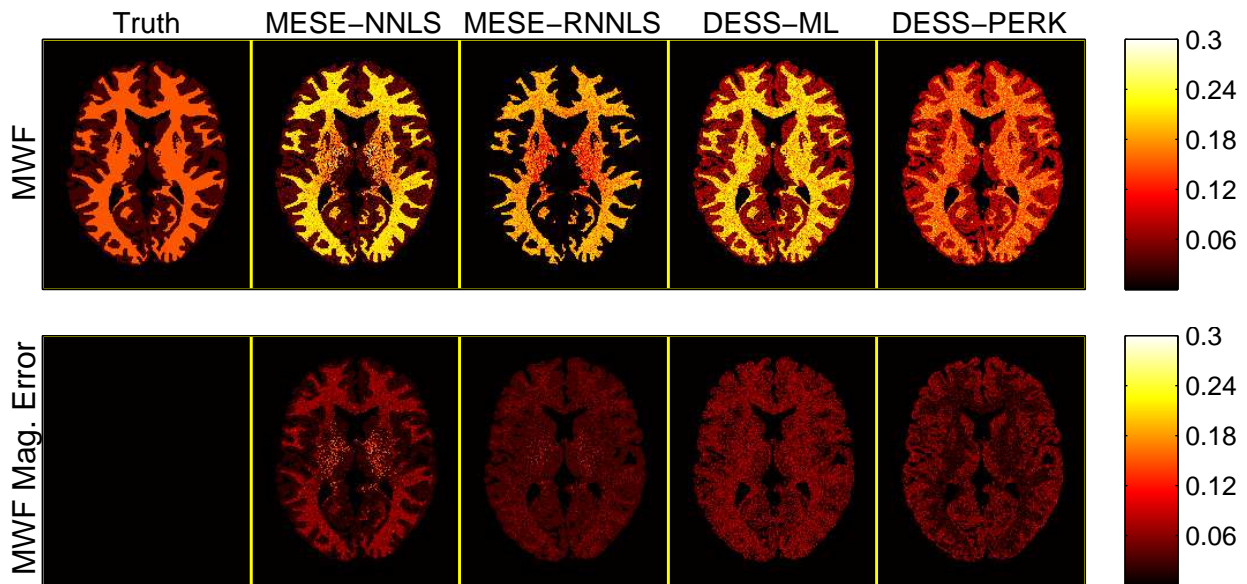


Figure S2: NNLS/RNNLS MESE f_M and ML/PERK DESS f_F estimates alongside corresponding magnitude error images, in a three-compartment simulation where any of the associated estimators could incur bias due to model mismatch. Voxels not assigned WM- or GM-like compartmental fractions are masked out in post-processing for display. Table S2 presents corresponding sample statistics.

S-II.B Three-Compartment Simulation with Model Mismatch

We next simulated data to arise from three non-exchanging water compartments with myelin water-like (500, 20)ms, cellular water-like (1000, 80)ms, and free water-like (3000, 3000)ms (longitudinal, transverse) relaxation time constants selected based on [6, 18]. With this three-compartment ground truth, the aforementioned MESE MWF estimators could incur bias due to their bulk- T_1 assumption and the aforementioned DESS fast-fraction estimators could incur bias due to their two-compartment assumption. Thus f_M and f_F are not equivalent here and their estimates need not necessarily be comparable. We assigned (myelin, cellular, free) water-like fractions of (0.15, 0.82, 0.03) in WM, and (0.03, 0.94, 0.03) in GM. We simulated data otherwise exactly as detailed in §3.2 to yield MESE image datasets with SNR ranging from 24-795 in WM and 29-862 in GM and to yield DESS image datasets with SNR ranging from 24-221 in WM and 30-241 in GM, where SNR is computed via (9). We estimated f_M from noisy magnitude MESE images and known bulk T_1 and κ maps by solving NNLS (S1) and RNNLS (S2) problems as explained in §S-I.B. We estimated f_F from noisy magnitude DESS images and known κ maps using ML and PERK estimators, as explained in §S-I.A. NNLS and RNNLS respectively took 42.7s and 69.2s. ML estimation took 17681s (nearly 5h), while PERK training and testing respectively took 34.2s and 1.1s.

Fig. S2 compares NNLS and RNNLS f_M estimates as well as ML and PERK f_F estimates alongside magnitude difference images with respect to the ground truth MWF. The PERK f_F esti-

	WM	GM
True $f_M \equiv f_F$	0.15	0.03
MESE-NNLS \widehat{f}_M	0.1910 ± 0.0463 (0.0618)	0.0349 ± 0.0192 (0.0198)
MESE-RNNLS \widehat{f}_M	0.1699 ± 0.0354 (0.0406)	0.00272 ± 0.00673 (0.02809)
DESS-ML \widehat{f}_F	0.1987 ± 0.0275 (0.0559)	0.0632 ± 0.0280 (0.0434)
DESS-PERK \widehat{f}_F	0.1576 ± 0.0243 (0.0254)	0.0754 ± 0.0231 (0.0510)

Table S2: Sample means \pm sample standard deviations (RMSEs) of NNLS/RNNLS MESE f_M estimates and ML/PERK DESS f_F estimates in a three-compartment simulation where any of the associated estimators could incur bias due to model mismatch. Sample statistics are computed over 7810 WM-like and 9162 GM-like voxels. Each sample statistic is rounded off to the highest place value of its (unreported) standard error, computed via formulas in [51]. Fig. S2 presents corresponding images.

mator achieves the lowest errors in WM but overestimates in GM (as does the ML f_F estimator), causing reduced WM/GM contrast relative to other estimators. Unlike both f_F estimates, both f_M estimates visibly exhibit systematic error due to flip angle spatial variation, despite perfect knowledge of κ . All estimates are higher (though to varying degrees) than corresponding estimates presented in Fig. S1, indicating some sensitivity to model mismatch. Except for PERK f_F estimates in WM and RNNLS f_M estimates in GM, all estimates exhibit greater error than corresponding estimates presented in Fig. S1, indicating that in most cases model mismatch is detrimental to estimation performance.

Table S2 compares sample statistics of NNLS and RNNLS f_M estimates as well as ML and PERK f_F estimates, computed over the same WM-like and GM-like ROIs as in Table S1. Several estimates now differ from true values by more than one standard deviation, indicating significant bias due to model mismatch in these cases. The PERK f_F estimator is most accurate and achieves the lowest RMSE in WM, but also suffers from the highest RMSE in GM. The NNLS f_M estimator is most accurate and achieves the lowest RMSE in GM, but also suffers from the highest RMSE in WM. RNNLS f_M (PERK f_F) estimates are now both more accurate and more precise than NNLS f_M (ML f_F) estimates in WM, suggesting that regularization may be beneficial in cases of model mismatch. Perhaps surprisingly, RNNLS f_M and PERK f_F estimates do not differ significantly in WM (but do differ in GM) suggesting that these WM estimates may be comparable even when characterizing 3-compartment systems, at least for the nominal ground-truth values selected here.

S-III Further Discussion

Extended simulations provide evidence that PERK is well-suited for DESS f_F estimation. Idealized two-compartment simulations demonstrate that PERK and standard ML f_F estimators achieve comparable RMSE in WM- and GM-like voxels, but PERK is more than $500\times$ faster. More realistic three-compartment simulations reveal that conventional MESE f_M estimates are sensitive to unaccounted variable T_1 -recovery rates across compartments and accounted flip angle spatial variation while DESS f_F estimates are sensitive to relaxation in an unaccounted third compartment, though the DESS PERK f_F estimator is most robust in WM to these sources of model misspecifi-

cation errors.

Taken together with the results in [28], results herein also provide evidence that the PERK estimator can maintain good performance while scaling more gracefully with the number of unknowns per voxel L than conventional ML estimators. In an application with $L \leftarrow 3$ unknowns [28], PERK was consistently at least $140\times$ faster than two well-suited ML estimators and achieved comparable performance in simulation, phantom, and in vivo studies. In myelin water imaging simulations ($L \leftarrow 6$), PERK was consistently at least $500\times$ faster than an ML estimator achieved via unrealistically narrow grid search around the ground truth. In early myelin water imaging in vivo experiments on other precision-optimized SPGR/DESS datasets from the same healthy volunteer, PERK took comparable time ($\sim 1\text{m}$ including training) and produced similar f_{F} estimates as reported here while a more realistically-constrained grid search took about 68 CPU-days (running on 24 nodes of a computing cluster). We omitted in vivo and ex vivo ML results here because these early experiments produced poor ML f_{F} estimates, likely due to multiple global minima of the associated ML cost function. Since PERK training time scales negligibly with the number of voxels, all of these acceleration factors would scale roughly linearly with the number of reconstructed slices for full-volume parameter estimation problems.